

# On the conservative phase-field method with the N-component incompressible flows

Cite as: Phys. Fluids 35, 012120 (2023); <https://doi.org/10.1063/5.0135490>

Submitted: 20 November 2022 • Accepted: 04 January 2023 • Accepted Manuscript Online: 04 January 2023 • Published Online: 26 January 2023

 Qing Xia (夏青), Junxiang Yang (杨钧翔) and  Yibao Li (李义宝)



[View Online](#)



[Export Citation](#)



[CrossMark](#)

## ARTICLES YOU MAY BE INTERESTED IN

[Computational fluid dynamics investigation of bitumen residues in oil sands tailings transport in an industrial horizontal pipe](#)

[Physics of Fluids 35, 013340 \(2023\); https://doi.org/10.1063/5.0132129](#)

[Investigation of parameters and porous plug enhanced enrichment with field-amplified sample stacking in microchip](#)

[Physics of Fluids 35, 012017 \(2023\); https://doi.org/10.1063/5.0135314](#)

[Novel framework for reconstructing the velocity field of pump-jet propulsor by super-resolution and Bayesian method](#)

[Physics of Fluids 35, 017132 \(2023\); https://doi.org/10.1063/5.0135365](#)



## Physics of Fluids

Special Topic: Paint and Coating Physics

Submit Today!

# On the conservative phase-field method with the N-component incompressible flows

Cite as: Phys. Fluids 35, 012120 (2023); doi: 10.1063/5.0135490

Submitted: 20 November 2022 · Accepted: 4 January 2023 ·

Published Online: 26 January 2023



View Online



Export Citation



CrossMark

Qing Xia (夏青),<sup>1</sup> Junxiang Yang (杨钧翔),<sup>2</sup> and Yibao Li (李义宝)<sup>1,a)</sup>

## AFFILIATIONS

<sup>1</sup>School of Mathematics and Statistics, Xi'an Jiaotong University, Xi'an 710049, China

<sup>2</sup>School of Computer Sciences and Engineering, Sun Yat-Sen University, Guangzhou 510275, China

<sup>a)</sup>Author to whom correspondence should be addressed: [yibaoli@xjtu.edu.cn](mailto:yibaoli@xjtu.edu.cn). URL: <http://gr.xjtu.edu.cn/web/yibaoli>

## ABSTRACT

This paper presents a conservative Allen–Cahn model coupled with the incompressible Navier–Stokes equation for tracking the interface with the N-component immiscible fluids system. The proposed conservative phase-field model can track the interface with large deformation in divergence-free velocity fields. The erroneous estimation of the normal vector is a challenging numerical issue for the interface capturing due to the appearance of spurious oscillations. The improved phase-field-based method combines the nonlinear preprocessing operation guided by the level-set method with local artificial viscosity stabilization to improve the computation of the discrete normal vector. The interfaces between different immiscible components are replaced by the transition region with finite thickness in the continuous phase field. The surface tension effects are represented with the continuous surface tension force in the system, which is not limited by the number of components. The third-order Runge–Kutta time discretization and second-order spatial discretization are applied for the multi-component system. To eliminate the spurious oscillations caused by discontinuous and steep gradient for capturing the shocks and sharp interfaces, we apply the third-order weighted essentially non-oscillatory method for the advection term. Several quantitative results of numerical tests, such as error estimation with the proposed method, comparative tests with different methods, and convergence rate for classical benchmark test, have been performed to illustrate that our method works well for the interface tracing issue with high numerical accuracy. In addition, various representative qualitative tests have been presented to demonstrate the applicability of our method.

Published under an exclusive license by AIP Publishing. <https://doi.org/10.1063/5.0135490>

## NOMENCLATURE

E	Ginzburg–Landau free energy
F	Helmholtz free energy
Fr	Froude number
<b>g</b>	gravity field
<b>n</b> <sub>s</sub>	outward unit normal vector
N	number of components
p	pressure
Re	Reynolds number
$\mathbb{R}^d$	d-dimension Euclidean space
<b>sf</b>	individual surface tension
<b>SF</b>	continuous surface tension force
<i>sgn</i>	smeared sign function
<i>t</i>	time
T	temperature
<b>u</b>	instantaneous velocity
<b>x</b>	coordinate vector

<i>x</i>	coordinate in the x-direction
<i>y</i>	coordinate in the y-direction
<i>z</i>	coordinate in the z-direction
$\beta$	variable Lagrangian multiplier
$\gamma$	mobility parameter
$\delta$	Dirac delta function
$\Delta t$	temporal step
$\nabla$	gradient operator
$\nabla \cdot$	divergence operator
$\nabla^2$	Laplace operator
$\varepsilon$	gradient energy coefficient
$\eta$	variable viscosity
$\theta$	contact line angle
$\kappa$	thermal conductivity
$\nu_s$	stabilization viscosity
$\rho$	density
$\sigma$	surface tension coefficient
$\phi$	phase variable with the phase-field method

$\psi$	phase variable with the level-set method
$\Omega$	computational domain
$\partial\Omega$	boundary of computational domain
$\otimes$	tensor product

## I. INTRODUCTION

Establishing the multi-component system under the immiscible fluids framework is significant for a wide range of scientific and industrial processes, which have attracted expensive attention across a number of disciplines in recent years, such as the coupling computation for the phase transition of melt pool in additive manufacturing,<sup>1,2</sup> building neural transmission networks for biological systems,<sup>3,4</sup> scientific computation on arbitrary surfaces,<sup>5,6</sup> and the detection of the atmospheric flow phenomena.<sup>7,8</sup> Methods to these issues broadly fell within two systems,<sup>9</sup> i.e., interface capturing methods<sup>10,11</sup> with diffusive interfacial transition and meshless particle based interface tracking methods.<sup>12,13</sup> However, the Lagrangian tracking method was hard to handle with severely deformation and fragmentary interfacial profile with the incurred computational cost caused by frequent re-meshing. The Eulerian methods, including the volume-of-fluid (VOF) method,<sup>14,15</sup> the Boltzmann method,<sup>16</sup> the phase-field method,<sup>17,18</sup> the level-set (LS) method,<sup>19,20</sup> the conservative level-set method,<sup>21,22</sup> and the ghost fluid method,<sup>23,24</sup> implicitly captured the interface by using the auxiliary fields corresponding to different fluids, which reflected the deformation of multi-component fluids by variegating the velocity field. For this type of method, the diffusion and anti-diffusion terms maintained the diffuse interface with controllable thickness instead of performing explicit reconstruction of the interfacial transition. Kim and Lowengrub<sup>25</sup> proposed a phase-field-based model for ternary fluid flows. Under their framework, the complicated system was solved by a nonlinear multigrid/projection method. Dong<sup>26,27</sup> presented a physical formulation within the phase-field framework for simulating the mixture consisting of N immiscible fluids, which is completely decoupled and has linear algebraic computational complexity. Li *et al.*<sup>28</sup> used the level-set method via two different level-set functions, which captured the moving interfaces of three different immiscible fluids. Howard and Tartakovsky<sup>29</sup> developed a conservative level-set free-energy-based surface tension model for N-phase flow, which minimized the numerical overlaps of fluids and voids founded in the standard conservative level-set method. Furthermore, Zhang and Wang<sup>30</sup> developed a projection method based approach to describe the ternary fluid system on solid surface with moving contact lines. Their scheme is energy stable, which ensures stability of the scheme. However, there are many difficulties in establishing a high-order numerical system for the multi-component flow system despite long periodic research.<sup>31</sup> Compared with the traditional low order method, although the high-order method can produce more accurate results on the coarse mesh, it is sensitive to the Gibbs phenomenon<sup>32</sup> and produces unstable results associated with discontinuities and steep gradients.<sup>33</sup>

Recent developments of phase-field method received extensive attention in tracking interface between different phases, which has been widely applied to range of problems such as phase transitions,<sup>34</sup> topology optimization with fluids<sup>35,36</sup> and solids,<sup>37</sup> image analysis,<sup>38,39</sup> the motion by mean curvature flows,<sup>40</sup> and crystal growth.<sup>41,42</sup> The phase-field model can be divided into two flavors: the conservative Cahn–Hilliard (CH) model and the non-conservative Allen–Cahn (AC) model. Yue *et al.*<sup>43</sup> examined the CH diffusion on mass

conservation, even though the phase field is conserved globally. Guo *et al.*<sup>44</sup> investigated the diffuse interface model based on CH equation by using the  $C^0$  finite element method, which can deal with fracture problems with the aid of complex interface/boundary interaction conditions. Li *et al.*<sup>45</sup> presented a conservative model based on a modified CH equation with the interfacial profile correction term. This method simplified the gridding, discretization, and handling of topological changes with consideration of hyperbolic tangent property. Compared with the CH equation, the AC equation relies more on an extra constraint to maintain mass conservation. However, it is numerically easier to implement AC equation than CH equation since the computation of fourth-order derivative terms can be avoided. Joshi and Jaiman<sup>46</sup> presented an adaptive variational procedure for unstructured mesh to capture dynamic interfaces in the binary fluids system. They estimated the residual-based error and applied the newest vertex bisection algorithm to perform the adaptive refinement. Zheng *et al.*<sup>47</sup> developed a conservative phase-field method for interface capturing based on the lattice Boltzmann (LB) method, which incorporated the interface force between different fluids into the incompressible multi-component fluids system by a potential form. Kim *et al.*<sup>48</sup> applied the space–time-dependent Lagrange multiplier to keep the small features and propose an unconditionally stable scheme for accurately calculating geometric features of sharp interface. Using the CH equation makes the sharp interface and shocks distorted, while the AC equation avoids over smooth and unphysical interface deformation. Lee and Kim<sup>49</sup> proved that the AC equation can keep the convex initial interface without self-intersection. However, how to establish a conserved phase-field model for multi-component systems and keep the shocks and sharp interface with steep gradient while considering the continuous surface tension effect between different interfacial profiles remain to be studied.

Let us focus on the following conventional AC equation:

$$\frac{\partial \phi}{\partial t} = \gamma \left( \nabla^2 \phi - \frac{F'(\phi)}{\varepsilon^2} \right), \quad (1)$$

where  $\phi$  is the phase variable and  $F(\phi)$  is the Helmholtz free energy with double well form. The parameters  $\gamma$  and  $\varepsilon$  define the regularized and finite thickness width parameters, respectively. The above equation fails to conserve the mass during the computation, which violates the physical context. To alleviate this disadvantage, several fruitful methods have been proposed for the modification of Eq. (1). Rubinstein and Sternberg<sup>50</sup> used the time-dependent Lagrange multiplier to compel mass conservation with the nonlocal AC equation, and Brassel and Bretin<sup>51</sup> used the space–time-dependent Lagrange multiplier to obtain better volume preserving properties. Chiu and Lin<sup>52</sup> reformulated the original AC equation and incorporated an anti-diffusive term to Eq. (1) as a conservative form

$$\frac{\partial \phi}{\partial t} = \gamma \left( \varepsilon \nabla \cdot (\nabla \phi) - \nabla \cdot \left( \phi(1-\phi) \frac{\nabla \phi}{|\nabla \phi|} \right) \right) \quad (2)$$

with the kernel functions  $\phi = 0.5 + 0.5 \tanh(\psi/(2\varepsilon))$ , where  $\psi$  is the signed distance function. However, the modified conservative AC equation is affected by the stiffness property. The choice of  $\gamma$  has tuned on the specific situation, which is caused by the false diffusion.<sup>53</sup> By drawing on the idea of the conservative level-set method, Chiu<sup>54</sup> proposed an alternative formulation to track the interface and developed

a nonlinear preconditioning phase-field equation for the conservative AC equation. However, the ill-conditioning of the normal vector causes erroneous estimate of interfacial profile due to the re-initialization equation. To avoid this issue, Al-Salami *et al.*<sup>9</sup> applied the high-order Flux Reconstruction approach on unstructured grids for capturing sharp interfaces. They resorted to the nonlinear preconditioning equation with localized artificial viscosity stabilization by coupling the level-set method with the phase-field method to alleviate the challenges of erroneous normal vectors and interface curvature. Inspired by the motivation of the alternative preconditioning method, we extend the binary fluids system under the conservative AC framework to the multi-component immiscible fluids system.

In this paper, we present a consistent and conservative system, which couples the incompressible Navier–Stokes equation and the AC equation, and apply it to a N-component immiscible fluids system based on the phase-field model. The main challenges faced by the high-order method for the multi-component system are summarized as follows: (i) The erroneous estimation of the normal vector is a tough numerical issue for the interface capturing due to the appearance of spurious oscillations. (ii) Few theoretical and numerical studies have considered the effect of continuum surface tension on multi-component hydrodynamic systems. (iii) It is hard to discretize the nonlinear inertial terms of the conserved form and consider the discontinuous properties of the cross-interface momentum. To overcome these issues, we couple the nonlinear preprocessing operation, which is guided by the level-set method using a local artificial viscosity stabilization, with the improved phase-field-based model to improve the computation of the discrete normal vector. Comparing to the existing incompressible interface tracking method, such as the volume of fluids method (VOF), the level-set (LS) method, and the lattice Boltzmann (LB) method, our method preserves the smooth evolution of the phase field (PF) method and provides the accurate partition guided by the LS and VOF methods to overcome the nonphysical dissipation caused by the interface thickness. The pressure and velocity field are fully coupled with the continuous phase field in the hybrid system, which represents the interfaces between different immiscible components by the transition region with finite thickness. Since the representation of surface tension is treated as a continuous force per unit volume, the surface tension effects between any combination of interfaces are not limited by the number of components. Furthermore, the four-stage third-order Runge–Kutta (RK) time discretization and second-order spatial discretization have been applied for the N-component system. The third-order weighted essentially non-oscillatory (WENO) spatial discretization has been applied with the advection term for capturing the shocks and sharp interfaces to eliminate the spurious oscillations caused by discontinuous and steep gradient. The proposed conservative model, which is a hybrid method by combining the level-set type surface tension formulation and normal vector modification with the phase-field type concentration relaxation, can track the interface with large deformation in divergence-free velocity fields of the N-component immiscible system. Various representative computational tests will be applied to demonstrate the applicability and high accuracy.

The outline of this paper is as follows. In Sec. II, we briefly review the methodology for the mixture of  $N$  incompressible immiscible fluids system. In Sec. III, a fully discrete, decoupled, explicit finite difference scheme will be performed for the  $N$ -component system. Section

IV is devoted to present various numerical experiments. Finally, concluding remarks are drawn in Sec. V.

## II. DESCRIPTION FOR THE MIXTURE OF N-INCOMPRESSIBLE IMMISCIBLE FLUIDS

Let us first investigate the evolution of the N-component conservative phase-field model on the domain  $\Omega \subset \mathbb{R}^d$ ,  $d = 1, 2, 3$ . If  $\Phi = (\phi_1, \dots, \phi_N)$  is the phase variables, which is the mole fractions of the different components, then the total mole fraction satisfies  $\sum_{i=1}^N \phi_i = 1$ , and the admissible states belong to the Gibbs N-component  $G := \left\{ \Phi \in \mathbb{R}^N \mid \sum_{i=1}^N \phi_i = 1, 0 \leq \phi_i \leq 1 \right\}$ . Let us begin with the Ginzburg–Landau free energy,

$$\mathcal{E}(\Phi) := \sum_{i=1}^N \mathcal{E}_i = \sum_{i=1}^N \int_{\Omega} \left( \frac{F(\phi_i)}{\varepsilon^2} + \frac{1}{2} |\nabla \phi_i|^2 \right) dx, \quad (3)$$

where  $F(\phi_i) = 0.5\phi_i^2(1 - \phi_i)^2$  and  $\varepsilon$  is the gradient energy coefficient which controls the width of the diffusive interface. We derive the AC equation, which was originally introduced as the phenomenological model, by taking the  $L_2$ -gradient flow of the total free energy  $\mathcal{E}(\Phi)$  as

$$\begin{aligned} & \frac{d}{d\xi} \mathcal{E}_i(\phi_i + \xi\theta)|_{\xi=0} \\ &= \int_{\Omega} \left( \theta \frac{F'(\phi_i)}{\varepsilon^2} + \nabla \theta \cdot \nabla \phi_i \right) dx \\ &= \int_{\Omega} \left( \frac{F'(\phi_i)}{\varepsilon^2} - \Delta \phi_i \right) \theta dx + \int_{\partial\Omega} \frac{\partial \phi_i}{\partial \mathbf{n}_S} \theta ds \\ &= \int_{\Omega} \left( \frac{F'(\phi_i)}{\varepsilon^2} - \Delta \phi_i \right) \theta dx. \end{aligned} \quad (4)$$

Thus, we derive the following AC equation with a double well potential:

$$\frac{\partial \phi_i}{\partial t} = \gamma \left( \nabla^2 \phi_i - \frac{F'(\phi_i)}{\varepsilon^2} \right), \quad (5)$$

where  $\gamma$  and  $\varepsilon$  are the mobility and smooth width parameter, respectively. Let us define the quantity  $\phi_i(\mathbf{x}, t)$  by signed distance function  $\psi_i$  as  $\phi_i = 0.5 + 0.5 \tanh(\psi_i/(2\sqrt{2}\varepsilon))$ . The above AC system has been proved by Ref. 48 that it cannot maintain the mass conservation during the computation. To avoid this disadvantage, we apply the counterterm approach<sup>57</sup> with Eq. (5) as

$$\frac{\partial \phi_i}{\partial t} = \gamma \left( \nabla^2 \phi_i - \frac{\phi_i(1 - \phi_i)(1 - 2\phi_i)}{\varepsilon^2} - |\nabla \phi_i| \nabla \cdot \left( \frac{\nabla \phi_i}{|\nabla \phi_i|} \right) \right). \quad (6)$$

Since the time evolution of  $\Phi$  is governed by gradient of the energy corresponding to the  $L_2$  inner product under the Gibbs condition, which should be hold everywhere during the computation, we added a variable Lagrangian multiplier  $\beta(\Phi)$  to Eq. (6). In addition, considering the convective effect caused by the fluids flow in the system, we add the convection term  $\mathbf{u} \cdot \nabla \phi_i$ , which leads to the following equation:

$$\begin{aligned} \frac{\partial \phi_i}{\partial t} + \mathbf{u} \cdot \nabla \phi_i &= \gamma \left( \nabla^2 \phi_i - \frac{\phi_i(1 - \phi_i)(1 - 2\phi_i)}{\varepsilon^2} \right. \\ &\quad \left. - |\nabla \phi_i| \nabla \cdot \left( \frac{\nabla \phi_i}{|\nabla \phi_i|} \right) + \beta(\Phi) \phi_i \right), \end{aligned} \quad (7)$$

where  $\mathbf{u}$  is the velocity of the fluids. Let us take the summation of Eq. (7) from  $i=1$  to  $i=N$ , and we want to keep  $\varphi = \sum_{i=1}^N \phi_i = 1$  to be the solution of the following equation:

$$\frac{\partial \varphi}{\partial t} + \mathbf{u} \cdot \nabla \varphi = \gamma \left( \nabla^2 \varphi - \sum_{i=1}^N \frac{\phi_i(1-\phi_i)(1-2\phi_i)}{\varepsilon^2} - \sum_{i=1}^N |\nabla \phi_i| \nabla \cdot \left( \frac{\nabla \phi_i}{|\nabla \phi_i|} \right) + \beta(\Phi) \right). \quad (8)$$

Since the left-hand side satisfies  $\partial \varphi / \partial t + \mathbf{u} \cdot \nabla \varphi = 0$ , we can derive

$$\beta(\Phi) = \sum_{i=1}^N \left( \frac{\phi_i(1-\phi_i)(1-2\phi_i)}{\varepsilon^2} + |\nabla \phi_i| \nabla \cdot \left( \frac{\nabla \phi_i}{|\nabla \phi_i|} \right) \right). \quad (9)$$

Based on the following expression,

$$\begin{cases} |\nabla \phi_i| = \frac{\partial \phi_i}{\partial \psi_i} = \frac{\phi_i(1-\phi_i)}{\varepsilon}, \\ \frac{(\nabla \phi_i \cdot \nabla) |\nabla \phi_i|}{|\nabla \phi_i|} = \frac{\partial^2 \phi_i}{\partial \psi_i^2} = \frac{\phi_i(1-\phi_i)(1-2\phi_i)}{\varepsilon^2}, \end{cases} \quad (10)$$

we can rewrite Eq. (7) as

$$\frac{\partial \phi_i}{\partial t} + \mathbf{u} \cdot \nabla \phi_i = \gamma \left( \nabla^2 \phi_i - \frac{1}{\varepsilon} \nabla \cdot (\phi_i(1-\phi_i) \mathbf{n}_S(\phi_i)) + \beta(\Phi) \phi_i \right), \quad (11)$$

where  $\mathbf{n}_S(\phi_i) = \nabla \phi_i / |\nabla \phi_i|$  is the outward unit normal vector to the interface of the two phases. As indicated by Al-Salami *et al.*<sup>9</sup>, choosing local multiplier for flow areas with exceptionally low velocity magnitudes yields better results. Additionally, the computational cost can be significantly reduced by using the local parameters with the global sweep of all degrees of freedom at each time step. Thus, we rewrite Eq. (11) as

$$\frac{\partial \phi_i}{\partial t} + \mathbf{u} \cdot \nabla \phi_i = \nabla \cdot (\tilde{\gamma} (\varepsilon \nabla \phi_i - \gamma^* \phi_i(1-\phi_i) \mathbf{n}_S(\phi_i))) + \gamma^* \beta(\Phi) \phi_i, \quad (12)$$

where  $\tilde{\gamma} = \max(\gamma^*, |\mathbf{u}|)$  and  $\gamma^*$  is the stabilized parameter. Based on the alternative preconditioning method, the interface displacement can be minimized by the level-set re-initialization. Therefore, the normal vector in Eq. (12) can be instead computed with  $\psi_i$  such that  $\mathbf{n}_S = \nabla \psi_i / |\nabla \psi_i|$ , and  $\psi_i$  can be obtained by the following stabilized preconditioning equation:

$$\frac{\partial \psi_i}{\partial t} + \text{sgn}(\psi^0) (1 - |\nabla \psi_i|) = \nabla \cdot (\nu_S \nabla \psi_i), \quad (13)$$

where  $\text{sgn}(\psi_i^0) = \tanh(\zeta \psi_i^0 / |\nabla \psi_i^0|)$  is a smeared sign function,  $\nu_S$  is the stabilization viscosity, and  $\zeta$  is the interface sharpness parameter.

We propose the conservative phase-field method for incompressible fluids

$$\frac{\partial(\rho \mathbf{u})}{\partial t} + \nabla \cdot (\rho \mathbf{u} \otimes \mathbf{u}) = -\nabla p + \frac{1}{Re} \nabla \cdot (\eta (\nabla \mathbf{u} + \nabla \mathbf{u}^T)) + \mathbf{SF} + \frac{\rho}{Fr} \mathbf{g}, \quad (14a)$$

$$\nabla \cdot \mathbf{u} = 0, \quad (14b)$$

$$\frac{\partial \phi_i}{\partial t} + \mathbf{u} \cdot \nabla \phi_i = \nabla \cdot (\tilde{\gamma} (\varepsilon \nabla \phi_i - \gamma^* \phi_i(1-\phi_i) \mathbf{n}_S(\phi_i))) + \gamma^* \beta \phi_i, \quad (14c)$$

$$\mathbf{n}_S = \frac{\nabla \psi_i}{|\nabla \psi_i|}, \quad (14d)$$

$$\frac{\partial \psi_i}{\partial t} + \text{sgn}(\psi^0) (1 - |\nabla \psi_i|) = \nabla \cdot (\nu_S \nabla \psi_i). \quad (14e)$$

where  $\mathbf{u}(\mathbf{x}, t)$  is the velocity field,  $p(\mathbf{x}, t)$  is the pressure field, the term  $\mathbf{u} \otimes \mathbf{u}$  is the tensor product,  $\rho(\Phi) = (\sum_{i=1}^N \phi_i / \rho_i)^{-1}$  is the variable density,  $\eta(\Phi) = (\sum_{i=1}^N \phi_i / \eta_i)^{-1}$  is the variable viscosity,  $Re$  is the Reynolds number, and  $\mathbf{SF}(\Phi)$  is the generalized continuous surface tension force for our multi-component fluid system, which can be summarized as

$$\mathbf{SF}(\Phi) := \sum_{i=1}^{N-1} \left( \sum_{j=i+1}^N \frac{\sigma_{ij}}{2} (\mathbf{sf}(\phi_i) + \mathbf{sf}(\phi_j)) \delta(\phi_i, \phi_j) \right). \quad (15)$$

Here,  $\sigma_{ij}$  denotes the surface tension coefficients,  $\mathbf{sf}(\phi_i) = -\kappa \varepsilon \nabla \cdot (\nabla \phi_i / |\nabla \phi_i|) |\nabla \phi_i| \nabla \phi_i$  is the individual surface tension, and  $\delta(\phi_i, \phi_j) = 5\phi_i \phi_j$  is the Dirac delta function, which has been used in Ref. 45 to combine the two different phases. The phase-field equation with the chemical potential form [Eq. (14c)] causes  $\phi_i = 1 - \phi_j$  to be satisfied at the interface between  $\phi_i$  and  $\phi_j$ . We should note that our system is not influenced by the over-determined problem, which has the generality with respect to the number of the fluid components. In order to design the surface tension for the sharp interface model, let us derive  $\kappa$  from

$$\int_{-\infty}^{\infty} \int_{-\infty}^{\infty} \varepsilon \kappa |\phi_x^e|^2 dx = 1, \quad (16)$$

where  $\phi_x^e(\mathbf{x}) = 0.5 + 0.5 \tanh(x / (2\sqrt{2}\varepsilon))$  is the equilibrium phase profile. Thus, we obtain  $\kappa = 6\sqrt{2}$  by taking the computation

$$\int_{-\infty}^{\infty} \int_{-\infty}^{\infty} \varepsilon \kappa |\phi_x^e|^2 dx = \int_{-\infty}^{\infty} \int_{-\infty}^{\infty} \frac{\kappa}{32\varepsilon} \operatorname{sech}^4 \frac{x}{2\sqrt{2}\varepsilon} dx = \frac{\kappa}{6\sqrt{2}}.$$

### III. DESCRIPTION OF THE NUMERICAL SOLUTION

The numerical solution of our N-component immiscible fluids system uses the second-order accurate spatial discretization and a third-order accurate temporal discretization. We present the numerical method in two dimension, which can be extended to three dimension in a straightforward manner without loss of generalities. We have to note that the computation is applied with  $\phi_1, \phi_2, \dots, \phi_{N-1}$ , since  $\phi_N = 1 - \sum_{i=1}^{N-1} \phi_i$  for the N-component AC system. Let us discretize the bounded domain  $\Omega = [a, b] \times [c, d] \subset \mathbb{R}^2$  as  $\Omega_d = \{(x_i, y_i) : 1 \leq i \leq N_x, 1 \leq i \leq N_y\}$ , where  $N_x$  and  $N_y$  are even integers and satisfy

$$\begin{aligned} a &= x_{\frac{1}{2}} < x_{1+\frac{1}{2}} < \dots < x_{N_x-1+\frac{1}{2}} < x_{N_x+\frac{1}{2}} = b, \\ c &= y_{\frac{1}{2}} < y_{1+\frac{1}{2}} < \dots < y_{N_y-1+\frac{1}{2}} < y_{N_y+\frac{1}{2}} = d. \end{aligned} \quad (17)$$

We assume that the partitions are uniform with grid size  $h$ . Thus, the center of each cell  $\Omega_{ij}$  can be denoted as  $(x_{i+\frac{1}{2}}, y_{j+\frac{1}{2}}) := (ih, jh)$ . We denote  $\phi_k^n$  as the approximation of the concentration of the  $k$ th component at time  $n\Delta t$ , where  $\Delta t = T/N_t$  is the time step with the total

computational time  $T$  and the number of computational time steps  $N_t$ . Let us use  $u_{ij}^n$ ,  $v_{ij}^n$ ,  $p_{ij}^n$ , and  $\phi_{ij}^n$  to denote the discrete approximations of  $u(\mathbf{x}_{ij}, n\Delta t)$ ,  $v(\mathbf{x}_{ij}, n\Delta t)$ ,  $p(\mathbf{x}_{ij}, n\Delta t)$ , and  $\phi(\mathbf{x}_{ij}, n\Delta t)$ , respectively. We shall consider the governing equation in two-dimensional space

$$\frac{\rho^{n+1}\mathbf{u}^{n+1} - \rho^n\mathbf{u}^n}{\Delta t} = -\nabla_d \cdot (\rho^n \mathbf{u}^n \otimes \mathbf{u}^n) - \nabla_d p^{n+1} + \frac{1}{Re} \nabla_d \cdot (\eta^n (\nabla_d \mathbf{u}^n + (\nabla_d \mathbf{u}^n)^T)) + \mathbf{SF}^n, \quad (18a)$$

$$\nabla_d \cdot \mathbf{u}^{n+1} = 0, \quad (18b)$$

$$\frac{\phi_i^{n+1} - \phi_i^n}{\Delta t} + \mathbf{u}^{n+1} \cdot \nabla_d \phi_i^n = \nabla_d \cdot (\tilde{\gamma} (\varepsilon \nabla_d \phi_i^n - \gamma^* \phi_i^n (1 - \phi_i^n) \mathbf{n}_S(\phi_i^n))) + \gamma^* \beta^n \phi_i^n. \quad (18c)$$

where  $\nabla_d$  and  $\nabla_d \cdot$  are the discrete gradient and divergence operators, respectively. In order to eliminate the numerical oscillation caused by the strong convective effect, we apply a mixed central WENO scheme to discretize the nonlinear inertial term with the conservative form on a staggered grid by following the general procedure proposed in Refs. 59 and 60. For obtaining a high-order accuracy of temporal discretization, we perform a four-stage third total variation distance (TVD) Runge-Kutta (RK) method, which has been widely used in single- or multi-phase flows. We obtain the intermediate velocity field based on the modified momentum equations, which can be decomposed into the combination of a divergence-free scalar field and a scalar field related to pressure based on the Helmholtz decomposition.<sup>61</sup> The outline of the main procedure in one time step follows

- $\mathcal{S}_1$ : Initialize  $\Phi^0$  to satisfy  $\sum_{i=1}^N \phi_i^0 = 1$  and  $\mathbf{u}^0$  to be the divergence-free velocity field.
- $\mathcal{S}_2$ : Without the consideration of pressure field, we compute the intermediate velocity field  $\mathbf{u}^*$ , which does not satisfy the incompressible condition

$$\begin{cases} \frac{\rho^{n+1}u^* - \rho^n u^n}{\Delta t} = -\left( (\rho^n(u^n)^2)_x + (\rho^n u^n v^n)_y \right) \\ \qquad \qquad \qquad + \frac{1}{Re} \left( (2\eta^n u_x)_x + (\eta^n(v_x + u_y))_y \right) + \mathbf{SF}_x^n, \\ \frac{\rho^{n+1}v^* - \rho^n v^n}{\Delta t} = -\left( (\rho^n u^n v^n)_x + (\rho^n(v^n)^2)_y \right) \\ \qquad \qquad \qquad + \frac{1}{Re} \left( (\eta^n(v_x + u_y))_x + (2\eta^n v_y)_y \right) + \mathbf{SF}_y^n, \end{cases}$$

where  $\mathbf{SF}^n = (\mathbf{SF}_x^n, \mathbf{SF}_y^n)$ . Let us consider the Runge-Kutta flux as

$$\begin{aligned} g(u^n, v^n) &= -\left( (\rho^n(u^n)^2)_x + (\rho^n u^n v^n)_y \right) \\ &\quad + \frac{1}{Re} D_u(\eta^n, \mathbf{u}^n) + \mathbf{SF}_x^n, \\ q(u^n, v^n) &= -\left( (\rho^n u^n v^n)_x + (\rho^n(v^n)^2)_y \right) \\ &\quad + \frac{1}{Re} D_v(\eta^n, \mathbf{u}^n) + \mathbf{SF}_y^n, \end{aligned} \quad (19)$$

where

$$\begin{aligned} D_u(\eta^n, \mathbf{u}^n)_{ij} &= (2\eta^n u_x^n)_x + (\eta^n(v_x^n + u_y^n))_y \\ &= \frac{1}{h^2} ((\eta_{i+1,j}^n + \eta_{ij}^n)(u_{i+1,j}^n - u_{ij}^n) \\ &\quad - (\eta_{ij}^n + \eta_{i-1,j}^n)(u_{ij}^n - u_{i-1,j}^n)) \\ &\quad + \frac{1}{2h^2} ((\eta_{ij}^n + \eta_{i,j+1}^n)(u_{i,j+1}^n - u_{ij}^n) \\ &\quad - (\eta_{ij}^n + \eta_{i,j-1}^n)(u_{ij}^n - u_{i,j-1}^n)) \\ &\quad + \frac{1}{8h^2} ((\eta_{ij}^n + \eta_{i,j+1}^n)(v_{i+1,j}^n - v_{i-1,j}^n + v_{i+1,j+1}^n - v_{i-1,j+1}^n) \\ &\quad - (\eta_{ij}^n + \eta_{i,j-1}^n)(v_{i+1,j}^n - v_{i-1,j}^n + v_{i+1,j-1}^n - v_{i-1,j-1}^n)), \end{aligned}$$

$$\begin{aligned} D_v(\eta^n, \mathbf{u}^n)_{ij} &= (\eta^n(v_x^n + u_y^n))_x + (2\eta^n v_y^n)_y \\ &= \frac{1}{h^2} ((\eta_{i,j+1}^n + \eta_{ij}^n)(v_{i,j+1}^n - v_{ij}^n) \\ &\quad - (\eta_{ij}^n + \eta_{i,j-1}^n)(v_{ij}^n - v_{i,j-1}^n)) \\ &\quad + \frac{1}{2h^2} ((\eta_{ij}^n + \eta_{i+1,j}^n)(v_{i+1,j}^n - v_{ij}^n) \\ &\quad - (\eta_{ij}^n + \eta_{i-1,j}^n)(v_{ij}^n - v_{i-1,j}^n)) \\ &\quad + \frac{1}{8h^2} ((\eta_{ij}^n + \eta_{i+1,j}^n)(u_{i,j+1}^n - u_{i,j-1}^n + u_{i+1,j+1}^n - u_{i+1,j-1}^n) \\ &\quad - (\eta_{ij}^n + \eta_{i-1,j}^n)(u_{i,j+1}^n - u_{i,j-1}^n + u_{i-1,j+1}^n - u_{i-1,j-1}^n)). \end{aligned}$$

Thus, the third-order RK method can be applied as follows:

$$\begin{aligned} u^{*,1} &= \frac{\rho^n}{\rho^{n+1}} u^n + \frac{\Delta t}{\rho^{n+1}} g(u^n, v^n), \\ v^{*,1} &= \frac{\rho^n}{\rho^{n+1}} v^n + \frac{\Delta t}{\rho^{n+1}} q(u^n, v^n), \\ u^{*,2} &= \frac{\rho^n}{2\rho^{n+1}} u^n + \frac{\rho^n}{2\rho^{n+1}} u^{*,1} + \frac{\Delta t}{2\rho^{n+1}} g^{*,1}, \\ v^{*,2} &= \frac{\rho^n}{2\rho^{n+1}} v^n + \frac{\rho^n}{2\rho^{n+1}} v^{*,1} + \frac{\Delta t}{2\rho^{n+1}} q^{*,1}, \\ u^* &= u^{*,2}, \quad v^* = v^{*,2}. \end{aligned} \quad (20)$$

- $\mathcal{S}_3$ : With the updated intermediate velocity field  $\mathbf{u}^*$ , we obtain the pressure field as

$$\left( \frac{p_x^{n+1}}{\rho^{n+1}} \right)_x + \left( \frac{p_y^{n+1}}{\rho^{n+1}} \right)_y = \frac{1}{\Delta t} (u_x^* + v_y^*) \quad (21)$$

by taking the multigrid method.

- $\mathcal{S}_4$ : With the obtained pressure field  $p^{n+1}$ , we compute the divergence-free normal velocity  $\mathbf{u}^{n+1}$  as

$$u^{n+1} = u^* - \frac{\Delta t p_x^{n+1}}{\rho^{n+1}}, \quad v^{n+1} = v^* - \frac{\Delta t p_y^{n+1}}{\rho^{n+1}}. \quad (22)$$

- $\mathcal{S}_5$ : Let us denote the right hand side of Eq. (18c) as

$$w(\phi^n) = \nabla_d \cdot (\tilde{\gamma} (\varepsilon \nabla_d \phi_i^n - \gamma^* \phi_i^n (1 - \phi_i^n) \mathbf{n}_S(\phi_i^n))) + \gamma^* \beta(\Phi^n) \phi_i^n, \quad (23)$$

$$\nabla_d \cdot \left( \frac{\nabla_d \phi}{|\nabla_d \phi|} \right)_{ij} = \frac{1}{2h} \left( \frac{\nabla_d \phi_{i+\frac{1}{2}, j+\frac{1}{2}}^x}{|\nabla_d \phi_{i+\frac{1}{2}, j+\frac{1}{2}}|} + \frac{\nabla_d \phi_{i+\frac{1}{2}, j-\frac{1}{2}}^x}{|\nabla_d \phi_{i+\frac{1}{2}, j-\frac{1}{2}}|} - \frac{\nabla_d \phi_{i-\frac{1}{2}, j+\frac{1}{2}}^x}{|\nabla_d \phi_{i-\frac{1}{2}, j+\frac{1}{2}}|} \right. \\ - \frac{\nabla_d \phi_{i-\frac{1}{2}, j-\frac{1}{2}}^x}{|\nabla_d \phi_{i-\frac{1}{2}, j-\frac{1}{2}}|} + \frac{\nabla_d \phi_{i+\frac{1}{2}, j+\frac{1}{2}}^y}{|\nabla_d \phi_{i+\frac{1}{2}, j+\frac{1}{2}}|} + \frac{\nabla_d \phi_{i-\frac{1}{2}, j+\frac{1}{2}}^y}{|\nabla_d \phi_{i-\frac{1}{2}, j+\frac{1}{2}}|} \\ \left. - \frac{\nabla_d \phi_{i+\frac{1}{2}, j-\frac{1}{2}}^y}{|\nabla_d \phi_{i+\frac{1}{2}, j-\frac{1}{2}}|} - \frac{\nabla_d \phi_{i-\frac{1}{2}, j-\frac{1}{2}}^y}{|\nabla_d \phi_{i-\frac{1}{2}, j-\frac{1}{2}}|} \right), \quad (24)$$

where

$$\nabla_d \phi_{i+\frac{1}{2}, j+\frac{1}{2}} = \left( \nabla_d^x \phi_{i+\frac{1}{2}, j+\frac{1}{2}}, \nabla_d^y \phi_{i+\frac{1}{2}, j+\frac{1}{2}} \right), \\ \nabla_d^x \phi_{i+\frac{1}{2}, j+\frac{1}{2}} = \frac{\phi_{i+1,j} + \phi_{i+1,j+1} - \phi_{ij} - \phi_{i,j+1}}{2h}, \quad (25) \\ \nabla_d^y \phi_{i+\frac{1}{2}, j+\frac{1}{2}} = \frac{\phi_{i,j+1} + \phi_{i+1,j+1} - \phi_{ij} - \phi_{i+1,j}}{2h}$$

thus, we give the four-stage third TVD Runge–Kutta method as follows:

$$\phi_i^{n,1} = \phi_i^n + \Delta t \left( w(\phi_i^n) - (u^{n+1} \phi_i^n + v^{n+1} \phi_i^n) \right), \quad (26a)$$

$$\phi_i^{n,2} = \frac{1}{2} \phi_i^n + \frac{1}{2} (\phi_i^{n,1} + \Delta t (w(\phi_i^{n,1}) - (u^{n+1} \phi_i^{n,1} + v^{n+1} \phi_i^{n,1}))), \quad (26b)$$

$$\phi_i^{n+1} = \phi_i^{n,2}. \quad (26c)$$

Unless otherwise stated, we use the Neumann boundary condition for the numerical simulation. Furthermore, the periodic boundary condition and the Dirichlet boundary condition can be applied.

Some notations should be summarized as follows: (i) Our discrete system Eq. (18) is solved by a third RK method for the temporal discretization. Under the second-order spatial discretization framework, we use the third-order WENO method<sup>31</sup> for the advection term to keep the sharp shock transitions in non-smooth region while obtaining the high-order accuracy in smooth regions. (ii) Our method alleviates the challenge of obtaining erroneous normal vectors and interface curvature by using the nonlinear preconditioning method. We need to reset  $\psi_i^0 = \phi_i - 1/2$  to be the initial condition of the stabilized equation (14e) in the beginning of the computation or the every  $N$  time steps. This operation does not involve much computational cost while prevents mass loss and produces accurate results. (iii) Our numerical scheme forces the interface transition, which can be represented by the explicit smoothing flow, to satisfy hyperbolic tangent property without mass loss. Meanwhile, the surface tension force computed by this method can neglect the influence of over-determined issue. (iv) For the linear equation (19), the computational complexities are  $O(N)$ , where  $N$  is the size of the mesh grid. For Poisson Eq. (21), we use the multigrid algorithm, which has  $O(N)$  computational complexity. For the computation of phase-field equation, we use the four-stage TVD method, which is linear and has  $O(N)$  computational complexity. Summarizing the aforementioned analysis, our method is simple and efficient to implement with low computational complexity. (v) Our computation is carried with the phase field model under the instructive guidance of the level-set method. By combining the advantages of these two methods, less numerical oscillation will be introduced into the system while capturing the interface. We use a conjugate gradient

algorithm with multigrid as preconditioner to accelerate the computation. Our computations are performed on a 3.6 GHz Intel Core with 16 GB of RAM loaded with C Language.

#### IV. COMPUTATIONAL VERIFICATION OF OUR MULTI-PHASE MODEL

In this section, we perform several interface tracing tests with background flows to validate that our method is, indeed, applicable and accurate under the multi-component framework. Furthermore, we apply various dynamic tests to demonstrate the robust capability of holding mass conservation law with hyperbolic tangent property and capturing the autonomously moving interface. We should note that the selection of the physical parameters in the proposed system can be chosen arbitrary, and our method is not restricted by the personalized selection.

##### A. Convergence test

Since there is no closed-form analytical solution for the coupled Navier–Stokes Allen–Cahn system, we should denote  $\phi^{\text{ref}}$ ,  $u^{\text{ref}}$ ,  $v^{\text{ref}}$ , and  $p^{\text{ref}}$  to be the reference solution obtained by a very fine time step for the spatial accuracy investigation or a very fine grid for the temporal accuracy investigation. We consider to investigate the convergence in a binary fluids flow system, and let us choose the initial condition as  $\mathcal{S}_1$  in the Appendix. The periodic boundary conditions have been applied for the accuracy test. The computational domain is chosen as  $\Omega_d = [0, 1] \times [0, 1]$  with a  $512 \times 512$  mesh grid, and we use the following parameters for the numerical simulations:  $\gamma = 0.5$ ,  $\nu_s = 1$ ,  $Re = 100$ , and  $\varepsilon = 5h/(4\sqrt{2}\tanh(0.9))$ . To demonstrate the third-order temporal accuracy, we perform the decreasing temporal steps as  $\Delta t = 1.0 \times 10^{-5}$ ,  $\Delta t = 5.0 \times 10^{-6}$ , and  $\Delta t = 2.5 \times 10^{-6}$  with the same spatial size  $h = 1/512$ . Let us define the reference solution as the results obtained by using the fine temporal step  $\Delta t = 1 \times 10^{-6}$ . The numerical error is defined as  $e_{i,\Delta t} := \phi_{i,\Delta t} - \phi_i^{\text{ref}}$ , and the rate of convergence is defined as  $\log_2(||e_{i,\Delta t}||_2 / ||e_{i,\Delta t/2}||_2)$ . As can be seen from Table I, our proposed method has third-order temporal accuracy, which corresponds to the discrete scheme Eqs. (20) and (26).

In order to show the spatial convergence rate, we perform the fixed temporal step size  $\Delta t = 1.0 \times 10^{-6}$  and apply the procedure until  $t = 0.1$ . The decreasing spatial steps are chosen as  $h = 1/128$ ,  $h = 1/256$ , and  $h = 1/512$ . The numerical spatial error is defined as  $e_{i,h} := \phi_{i,h} - \phi_i^{\text{ref}}$ , and the spatial convergence rate is defined as  $\log_2(||e_{i,h}||_2 / ||e_{i,h/2}||_2)$ . The reference solution is obtained using a very fine space grid size  $h = 1/1024$ . Table II shows the spatial convergence results, which has confirmed that the proposed method is, indeed, second-order accurate in space.

##### B. Parameters analysis

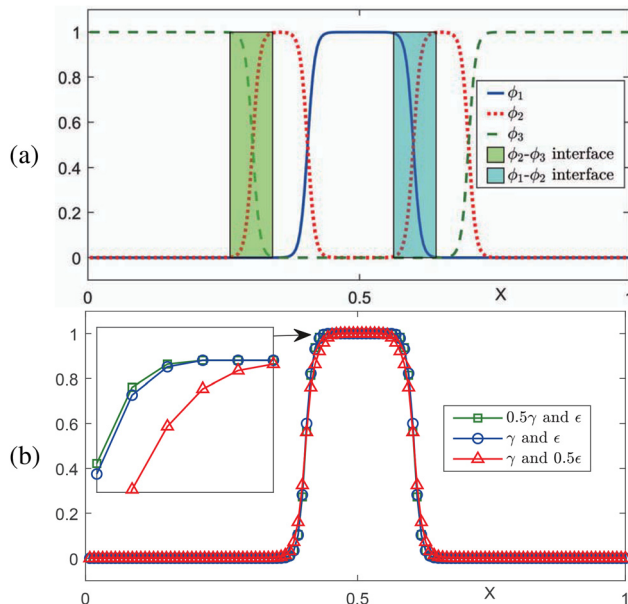
In this subsection, we investigate the influence of different parameters,  $\gamma$  and  $\varepsilon$ , and surface tension SF in our proposed method, which play a major role in the calculated results. Let us consider the dynamics of a droplet insider another elliptical drop embedded in the ambient liquid, which is consisted of ternary fluids flow. The computational domain is chosen as  $\Omega_d = [0, 1] \times [0, 1]$  with a  $512 \times 512$  mesh grid, and we set the initial condition as the  $\mathcal{S}_2$  in the Appendix. We set the parameters as follows:  $\gamma = 0.5$ ,  $\nu_s = 1$ ,  $Re = 100$ ,  $\varepsilon = 5h/(4\sqrt{2}\tanh(0.9))$ , and  $\Delta t = 5h^2$ . We first plot the cutlines of

**TABLE I.** Errors and convergence rates with different time steps for velocity fields  $u$  and  $v$ , pressure  $p$ , and phase field  $\phi$ .

$\Delta t$	Error				Order			
	$u$	$v$	$p$	$\phi$	$u$	$v$	$p$	$\phi$
$1.0 \times 10^{-5}$	$8.214 \times 10^{-04}$	$7.361 \times 10^{-04}$	$6.812 \times 10^{-04}$	$9.799 \times 10^{-04}$	...	...	...	...
$5.0 \times 10^{-6}$	$1.534 \times 10^{-04}$	$1.209 \times 10^{-04}$	$9.262 \times 10^{-05}$	$1.708 \times 10^{-04}$	2.42	2.58	2.88	2.52
$2.5 \times 10^{-6}$	$1.882 \times 10^{-05}$	$1.252 \times 10^{-05}$	$1.211 \times 10^{-05}$	$2.267 \times 10^{-05}$	3.03	3.30	2.94	2.91

**TABLE II.** Errors and convergence rates with different spatial steps for velocity field  $u$  and  $v$ , pressure  $p$ , and phase field  $\phi$ .

$N$	Error				Order			
	$u$	$v$	$p$	$\phi$	$u$	$v$	$p$	$\phi$
128	$2.755 \times 10^{-03}$	$3.732 \times 10^{-03}$	$6.582 \times 10^{-03}$	$3.721 \times 10^{-03}$	...	...	...	...
256	$7.256 \times 10^{-04}$	$9.594 \times 10^{-04}$	$1.671 \times 10^{-03}$	$8.988 \times 10^{-04}$	1.92	1.96	1.98	2.04
512	$1.569 \times 10^{-04}$	$2.252 \times 10^{-04}$	$3.988 \times 10^{-04}$	$1.876 \times 10^{-04}$	2.21	2.09	2.07	2.26

**FIG. 1.** Vertical cutline of phase fields at  $y = 0.5$ . (a) Cutlines for three phases. (b) Cutlines of  $\phi_1$  with different  $\epsilon$  and  $\gamma$  couples at the same indicated time.

three components in Fig. 1(a). As can be seen from the results, the shaded parts are the interface between the different phases since the phase-field method yields a thickness transition region, which is dependent on the parameter  $\epsilon$ . By choosing different combinations of  $\epsilon$  and  $\gamma$ , as shown in Fig. 1(b), we investigate their effect on the interfacial transition. We demonstrate the cutlines of  $\phi_1$ . Choosing different  $\gamma$  with the same  $\epsilon$  (the green line with squares and the blue line with circles) only influences the convergence rate, not the position and thickness of the interface, since  $\gamma$  is the constant mobility of the phase-field functional. Choosing different  $\epsilon$  with the same  $\gamma$  (the blue line

with circles and the red line with triangles) changes the thickness of the interfacial region. In order to explore the influence of surface tension on the dynamic of droplet, we consider to add a shear flow [ $u(x, y, 0) = 1 - 2y$ ,  $v(x, y, 0) = 0$ ] to the existing initial condition. We set the same parameters and plot the 0.5-level contour line to represent the interface profiles between the ternary liquids as shown in Fig. 2. It is obvious that the droplets are gradually stretched in the absence of surface tension. In contrast, the surface tension forces the droplets to hold the ellipse shape.

### C. Capillary filling model for moving contact line problems

In this subsection, we refer to the extensive work<sup>52</sup> for the investigation on capillary filling problem with multi-component. The capillary filling problem, which originated from the pioneering work of Washburn,<sup>53</sup> offers a good benchmark for assessing whether a multi-phase model is able to simulate moving contact line problems. Before the simulation is carried out, we first introduce the wetting boundary condition for the ternary fluid system. We define three static contact angles  $\theta_{12}$ ,  $\theta_{13}$ , and  $\theta_{23}$  of the wettability of the solid wall, respectively, which are related to the interfacial tension according to Young's equation as

$$\begin{cases} \sigma_{12} \cos \theta_{12} = \sigma_{2s} - \sigma_{1s}, \\ \sigma_{13} \cos \theta_{13} = \sigma_{1s} - \sigma_{3s}, \\ \sigma_{23} \cos \theta_{23} = \sigma_{3s} - \sigma_{2s}. \end{cases} \quad (27)$$

Here,  $\sigma_{is}$  ( $i = 1, 2, 3$ ) denotes the surface tension between fluid  $\phi_i$  and the solid. We denote  $\theta_{ij}$  ( $i, j = 1, 2, 3$ ) as the contact angle between the  $\phi_i - \phi_j$  interface. Thus, we have  $\theta_{ij} = \pi - \theta_{ji}$ , and the relationship between the static contact angles and interfacial tensions can be summarized as

$$\sigma_{12} \cos \theta_{12} + \sigma_{23} \cos \theta_{23} + \sigma_{13} \cos \theta_{13} = 0. \quad (28)$$

Thus, we only need to specify two contact angles, and the remaining angle can be calculated from Eq. (28). The boundary condition can be set as

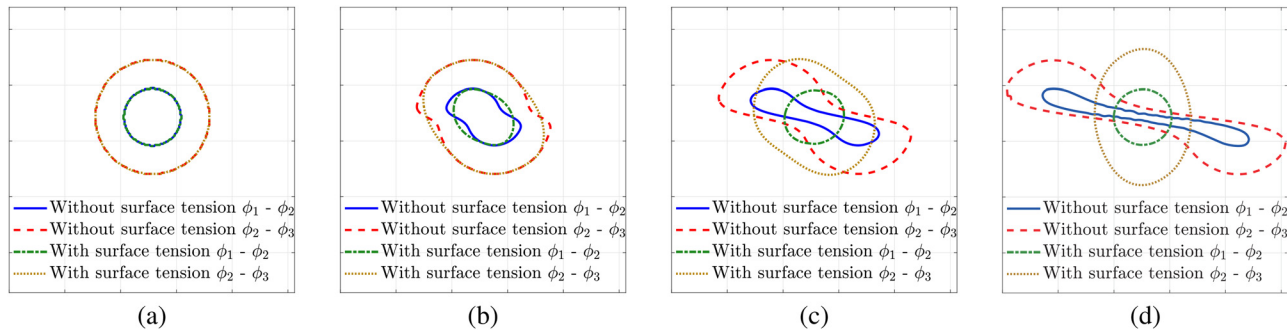


**FIG. 2.** Comparison results obtained by our method with and without surface tension. From (a) to (d), the indicated times are  $t = 0, 0.10, 0.20$ , and  $0.40$ , respectively.

$$\nabla \phi_i \cdot \mathbf{n}_s = -|\nabla \phi_i| \cos \theta_i = -\phi_i(\phi_i - 1) \cos \theta_i / (\sqrt{2}\varepsilon), \quad (29)$$

where  $\theta_i$  is the weighted contact angle of fluid  $\phi_i$ , and the weighted contact angle can be calculated as

$$\begin{cases} \theta_1 = (\theta_{12} + \theta_{13})/2, \\ \theta_2 = (\theta_{23} + \theta_{12})/2, \\ \theta_3 = (\theta_{13} + \theta_{23})/2. \end{cases} \quad (30)$$

Here, we assume that there is a capillary tube in 2D domain, which connects to the reservoir of  $\phi_1$  at the left inlet and connects to the reservoir of  $\phi_3$  at the right outlet. For the capillary tube, the hybrid system is consisted of ternary fluids flow, and we neglect the fluid inertia and consider that the spontaneous process is driven by capillary pressure. We choose the computational domain as  $[0, 4] \times [0, 1]$  with a  $1024 \times 256$  mesh grid and set the initial condition as  $\mathcal{S}_3$  in the Appendix. We selected several angle combinations to test our numerical model as shown in Table III. As can be seen from the results, our method can be applied to the simulation of moving contact lines for capillary filling problem. Furthermore, the analytical solution and the numerical solution are in good agreement.

#### D. Rotation under the background velocity field

We first investigate the interfacial transition under the influence of background velocity. To demonstrate the qualitative effect, we choose the computational domain as  $\Omega_d = [0, 1] \times [0, 1]$  with a  $512 \times 512$  mesh grid and the following parameters:  $\gamma = 0.45$ ,  $\nu_s = 0.8$ ,  $Re = 50$ ,  $\varepsilon = 5h/(4\sqrt{2}a \tanh(0.9))$ , and  $\Delta t = 0.5h^2$ . For this test, we consider the hybrid system with five components. We demonstrate the evolution of windmill rotation in Fig. 3. The initial conditions are chosen as  $\mathcal{F}_4$  in the Appendix. We show the initial

**TABLE III.** The comparison between the simulated contact angles and analytical contact angles with different viscosity settings.

	$\theta_1 : \theta_3$ (deg)		
$\eta_1 : \eta_2 : \eta_3$	60.00/30.00	45.00/60.00	75.00/25.00
1 : 0.5 : 0.1	59.14/31.03	44.73/58.95	74.10/24.94
1 : 0.5 : 0.5	60.82/29.71	44.02/60.19	74.47/26.07
1 : 0.1 : 0.1	59.95/29.73	45.27/59.62	75.39/25.21

velocity field in Fig. 3(a) and demonstrate the interface profiles of the multi-component system and its close-up view in Fig. 3(b). Figures 3(c)–3(e) show the evolution of the windmill rotation at indicated times 1/128, 1/64, and 1/32, respectively. As we expected, the windmill rotates for a quarter of a cycle by inverting the velocity field at the indicate time  $t = 1/32$ . It is obvious that there is no phase transition while the windmill rotates, which corresponds to the physical context. Comparing to the initial state, the multi-component system shrinks to satisfy the hyperbolic tangent property from the closed-view window. We should note that this contraction transformation does not influence the mass conservation of the individual component or the whole system, which will be verified in the subsequent numerical test. It can be seen from the aforementioned results that the proposed multi-component phase-field model works well for the sharp interface capturing. In order to quantitatively investigate the influence of our method on each component during computation, we calculate the errors of each component in the above process. Since the windmill can be returned to the initial position by inverting the background flow at time  $t = 1/8$ , the measurement value at the quarter period  $t = 1/32$  should theoretically remain the same as the initial value. We set the initial conditions  $\phi^0(i = 1, \dots, N)$  as the exact solutions and note that the ellipses should not change their shapes as a result of the rotation. Let us define the error of a grid as the discrete  $l_2$ -norm of the difference between the numerical solution and the exact solution for every single component as

$$e^k = \sqrt{\sum_{i=1}^{N_x} \sum_{j=1}^{N_y} (\phi_{i,j}^k - \phi_{i,j}^0)^2 / (N_x N_y)}, \quad (31)$$

where  $k = 1, \dots, N$  is defined as the index of components. Thus, we can calculate the error of the results:  $e^1 = 3.547 \times 10^{-5}$ ,  $e^2 = 5.210 \times 10^{-5}$ ,  $e^3 = 4.394 \times 10^{-5}$ ,  $e^4 = 3.924 \times 10^{-5}$ , and  $e^5 = 4.726 \times 10^{-4}$ . Obviously, these error values are small, and their summation is zero, which implies that the total mass is conservative.

Furthermore, we compare the results obtained by the reduction consistent multi-phase conservative Allen-Cahn model in Ref. 58 with our method to demonstrate that our system, indeed, conserves the mass and alleviates the loss of accuracy. We consider a novel system with four components, which can be initialized as  $\mathcal{F}_5$  in the Appendix. The comparison results have been demonstrated in Fig. 4. The initial velocity field and multiple phase field have been shown in Fig. 4(a). From Figs. 4(b)–4(d), we plot the 0.5-contour line of the results obtained by the conserved phase field (CPF) method and our proposed method at indicated times

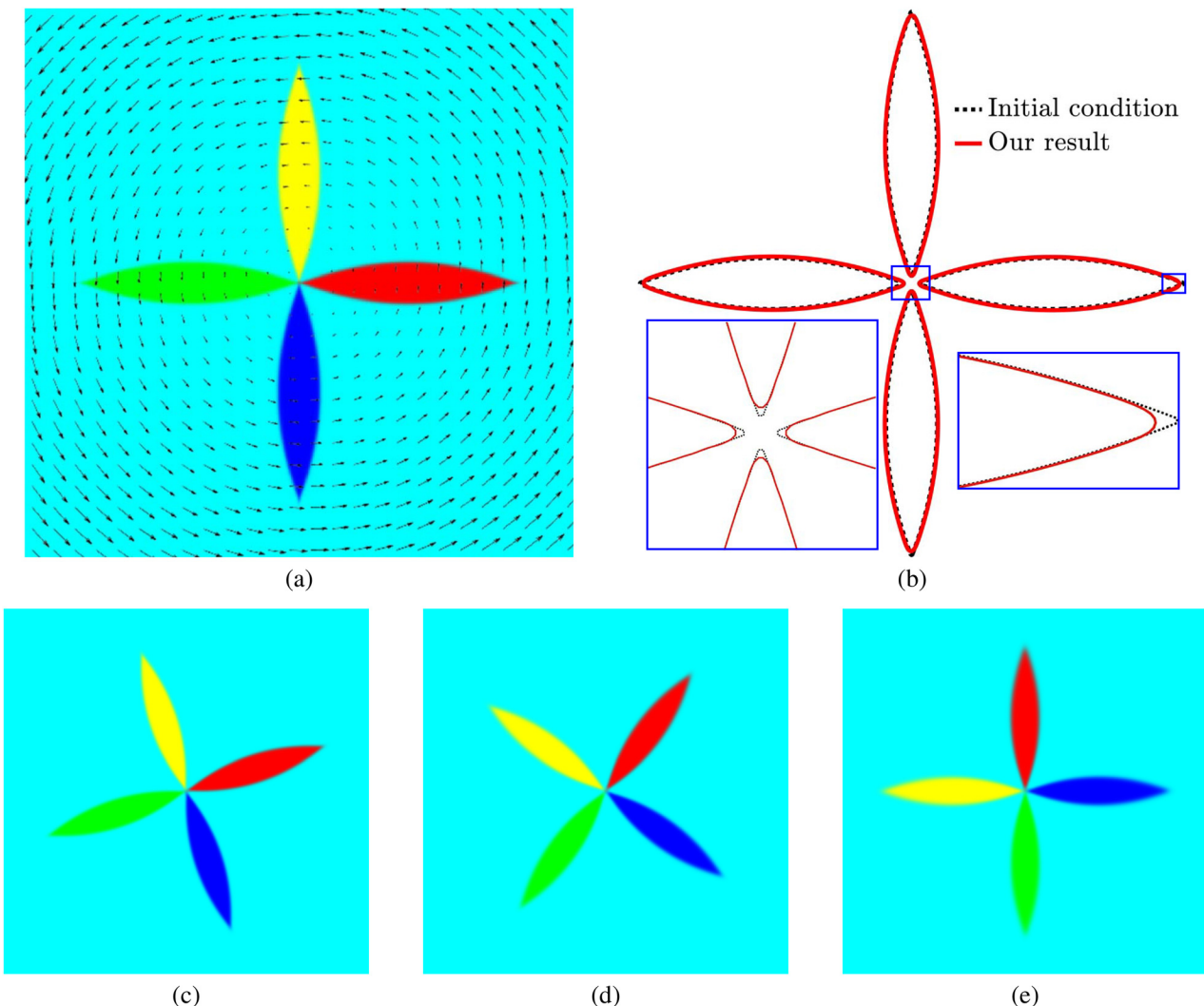


**FIG. 3.** Evolution of the rotation under the fix background velocity field. (a) The initial velocity field and phase field. (b) The interface profiles of the multi-component system and its close-up view. (c)–(e) The evolution of the windmill rotation.

$t = 1/128, 1/64$ , and  $1/32$ , respectively. The colored solid line is the exact result, the colored dotted line is the result obtained by our method, and the black dotted line is the result obtained by the proposed method in the work of Huang *et al.*<sup>58</sup> From the point of the whole system, the shape of each component does not change under the influence of background flow by the two methods. From the closed-view windows, the interfacial profile satisfies the hyperbolic tangent property under the impact of the surface tension force. We use Eq. (31) to compute every single phase error  $e_{CPF}^k$  and  $e_{Our}^k$  ( $k$  is the phase index) obtained by the CPF method and our method, respectively. We list the errors as follows:  $e_{CPF}^1 = 3.627 \times 10^{-5}$ ,  $e_{CPF}^2 = 4.416 \times 10^{-5}$ ,  $e_{CPF}^3 = 3.142 \times 10^{-5}$ ,  $e_{CPF}^4 = 5.272 \times 10^{-4}$ ,  $e_{Our}^1 = 1.218 \times 10^{-5}$ ,  $e_{Our}^2 = 3.173 \times 10^{-5}$ ,  $e_{Our}^3 = 2.756 \times 10^{-5}$ , and  $e_{Our}^4 = 9.564 \times 10^{-5}$ . The comparison results verify that our method can get more accurate results.

## E. Investigation of Rider–Kothe vortex

In this subsection, we investigate the capability of the proposed multi-component system with the Rider–Kothe (RK) vortex. The RK vortex benchmark case<sup>62</sup> is a typical example to verify the capability of the numerical method to track the interface under large deformation, which can investigate the validity of the numerical model by exploring droplet deformation in a rotating and stretching velocity field. The computational domain is chosen as  $\Omega = [0, 1] \times [0, 1]$  with a  $256 \times 256$  mesh grid. We choose the proper physical parameters as  $\gamma = 0.5$ ,  $\nu_s = 1.2$ ,  $Re = 50$ ,  $\epsilon = 5h/(4\sqrt{2}\tanh(0.9))$ , and  $\Delta t = 0.05h$ . The hybrid system is consisted of ternary fluid flows. The background flow is guided by a forward-then-backward velocity field, which forces the droplet to be stretched and comes back to the initial condition. Therefore, we can investigate the accuracy of the numerical method by

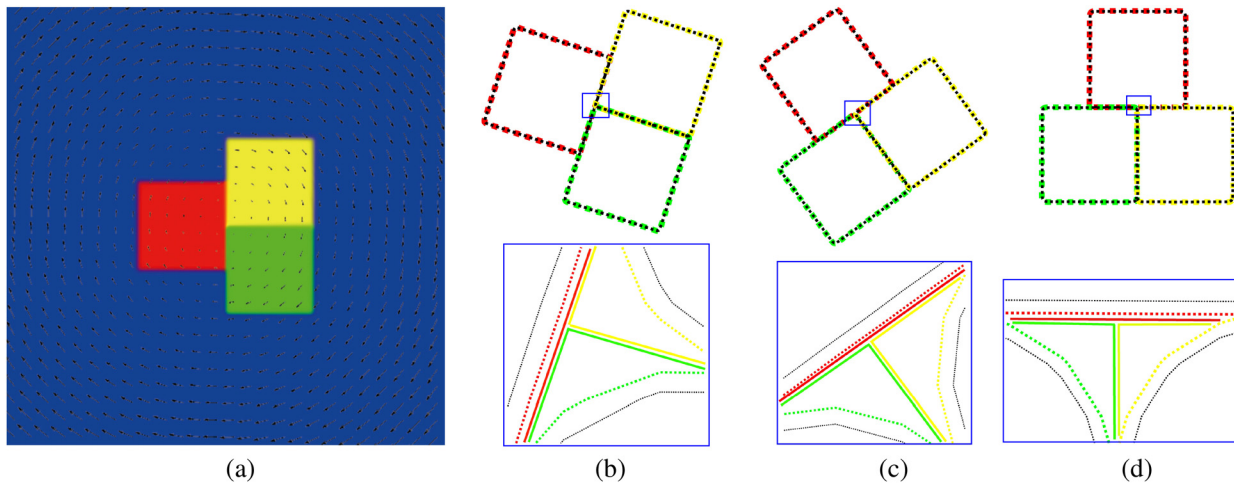


**FIG. 4.** Comparison of the results obtain by the CPF method and our method. (a) The initial velocity field and phase field. From (b)–(d), the indicated times are  $t = 1/128$ ,  $1/64$ , and  $1/32$ , respectively. We plot the 0.5-contour line of each component. The colored solid line is the exact result, the colored dotted line is the result obtained by our method, and the black dotted line is the result obtained by CPF method.

computing the deviation between the final and initial solution. We set the initial conditions for the ternary fluid flows system as  $\mathcal{F}_6$  in the [Appendix](#), with the time period  $T = 12$ . We have shown the evolution of the shape deformation in the RK vortex benchmark case in [Fig. 5](#). From [Figs. 5\(a\)–5\(d\)](#), the indicated times are  $t = 0$ ,  $T/4$ ,  $T/2$ , and  $T$ , respectively. It is obvious that the droplet is stretched at  $t = T/2$  to form a thin filament, which indicates that our method is able to capture the interfacial deformation during the stretching process without artifacts or instabilities. The comparison results shown in [Fig. 5\(d\)](#) demonstrate that there is an acceptable deviation between the final and initial solution of the multi-system.

We compute the errors of every single phase during the evolution with the following single mass error  $e_{evo}^k$  and total mass error  $e_{tot}$ :

$$e_{evo}^k = \left| \sum_{i=1}^{N_x} \sum_{j=1}^{N_y} \phi_{i,j}^k / (N_x N_y) - \sum_{i=1}^{N_x} \sum_{j=1}^{N_y} \phi_{i,j}^0 / (N_x N_y) \right|,$$

$$e_{tot} = \sum_{k=1}^N \left| \sum_{i=1}^{N_x} \sum_{j=1}^{N_y} \phi_{i,j}^k / (N_x N_y) - \sum_{i=1}^{N_x} \sum_{j=1}^{N_y} \phi_{i,j}^0 / (N_x N_y) \right|.$$

The quantitative measurements of the individual phase have been shown in [Fig. 6](#). The comparable results clearly indicate that our method can be effectively performed for the computation with acceptable mass loss. In [Table IV](#), we compare the quantitative measure of the MLP-UB + RK2 method in Ref. 55, the traditional PF method, the LS method, and the VOF method, and the CPF method in Ref. 54. We extend the CPF method for binary fluid flows to a multi-phase framework. The quantitative indexes to be explored are the average errors and convergence rates, where the average error can be calculated by Eq. (31). As can be seen from the quantitative results, the error of our method is, indeed, smaller although the convergence rates for the two methods are both with second-order accuracy. We apply the comparison results obtained by our method, the CPF method in Ref. 54, and the MLP-UB + RK2 method in Ref. 55 in [Fig. 7](#). We choose the same

initial conditions for this numerical investigation with [Fig. 5](#). The comparison results demonstrate that the conserved procedure in this work appears to be robust. Our method provides a satisfactory solution for the multi-phase RK variation problem.

#### F. Simulation of perturbation with Kelvin–Helmholtz instability

Performing the perturbation with Kelvin–Helmholtz (KH) instability, which is caused by the sufficiently large velocity difference, is a significant way to investigate the proposed algorithm.<sup>63,64</sup> In this subsection, we apply a small amplitude perturbed on the interfacial profiles between the four-component fluids. The surface tension force has been omitted for this simulation. In this case, we consider the hybrid system with four components, which can be initialized as  $\mathcal{F}_7$  in the [Appendix](#). The computational domain is chosen as  $\Omega = [0, 1] \times [0, 1]$  with a  $512 \times 512$  mesh grid. We choose the proper physical parameters as  $\gamma = 0.5$ ,  $\nu_s = 1.2$ ,  $\varepsilon = 5h/(4\sqrt{2}a \tanh(0.9))$ ,  $\Delta t = 0.05h$ ,  $Fr = 1$ , and  $\rho_1 : \rho_2 : \rho_3 : \rho_4 = 1 : 5 : 10 : 20$ . We apply the periodic boundary conditions for the left and right boundaries. For the top and bottom boundaries, we apply the homogeneous Neumann boundary conditions. In order to investigate the influence of Reynolds number, we choose  $Re = 5000$  and  $Re = 500$  to demonstrate the results as shown in [Fig. 8](#) at indicated times  $t = 0$ ,  $t = 0.1$ ,  $t = 0.3$ , and  $t = 0.5$ . The arrows on the diagram show the flow field. As can be seen from [Fig. 8](#), the result difference with the two Reynolds numbers is not obvious in the early stages of evolution. When the convection is dominant, the captured turbulence interfaces demonstrate different shapes. The perturbation is further developed with the increase in  $Re$ . It is obvious that our method can be directly used for the simulation of multi-component fluids flow with KH instability. In order to demonstrate that the results are dependent on the choice of initial conditions, we choose different combinations of perturbations as shown in [Fig. 9\(a\)](#) with the same initial conditions. Let us take the example of  $\phi_1$  and make the following changes in perturbations:

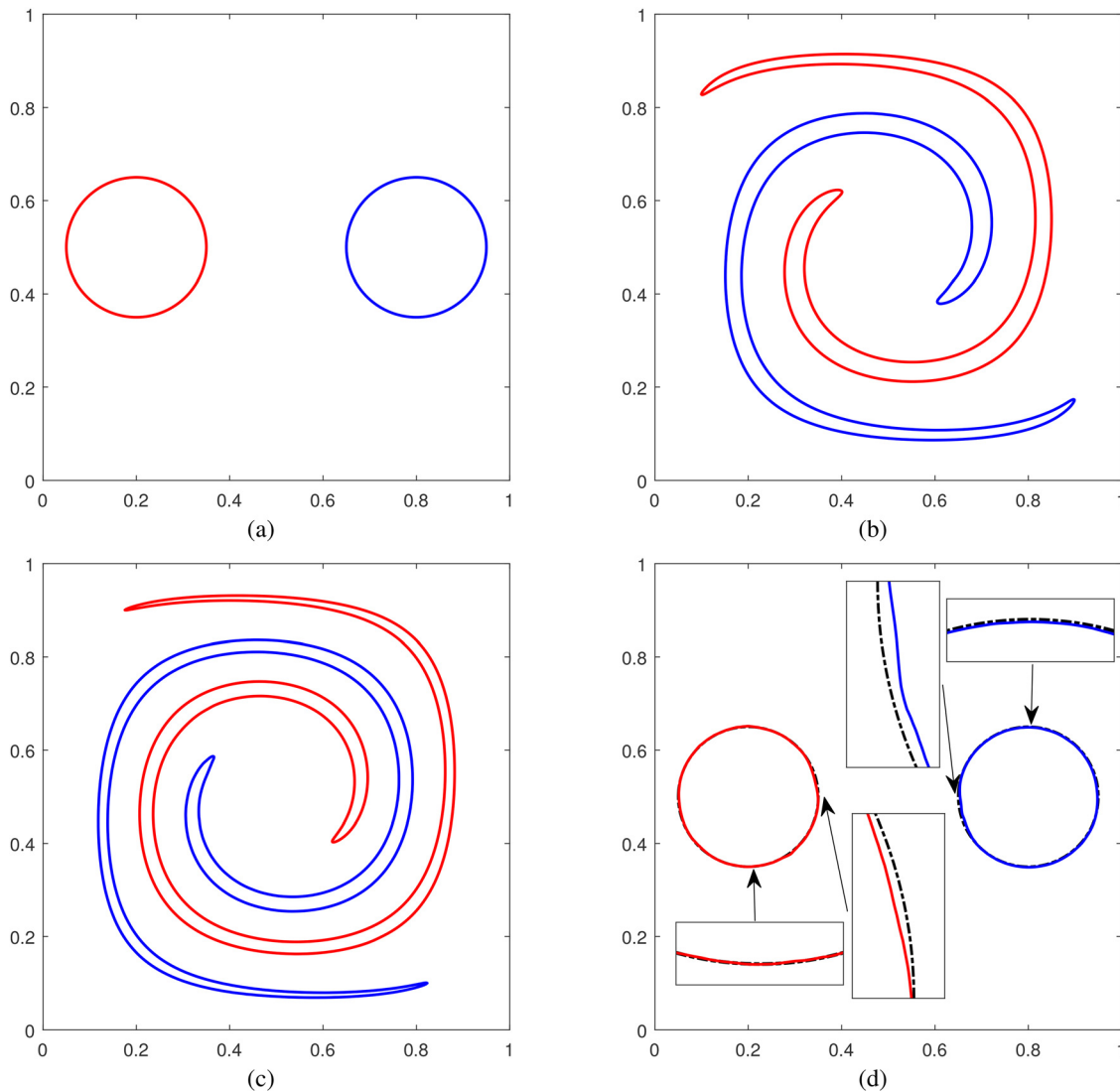


**FIG. 5.** The evolution of the shape deformation in the Rider–Kothe vortex benchmark case. From (a)–(d), the indicated times are  $t = 0$ ,  $T/4$ ,  $T/2$ , and  $T$ , respectively.

$$\text{IC 1 : } \phi_1(x, y, 0) = 0.5 + 0.5 \tanh\left(\frac{y - 0.75 - 0.01 \sin(4\pi x)}{2\sqrt{2}\epsilon}\right),$$

$$\text{IC 2 : } \phi_1(x, y, 0) = 0.5 + 0.5 \tanh\left(\frac{y - 0.75 - 0.05 \sin(4\pi x)}{2\sqrt{2}\epsilon}\right),$$

$$\text{IC 3 : } \phi_1(x, y, 0) = 0.5 + 0.5 \tanh\left(\frac{y - 0.75 - 0.1 \sin(4\pi x)}{2\sqrt{2}\epsilon}\right).$$

The results from Figs. 9(a)–9(c) are captured at the indicated times  $t = 0$ , 0.25, and 0.5, respectively. As can be seen from the results, different initial conditions are sensitive to the problem of simulating the interfacial transition of the KH instability.

#### G. Droplet hedging under the influence of gravity

In this subsection, we consider the ternary fluids system with two droplets. The computational domain is chosen as  $\Omega = [0, 0.5] \times [0, 1]$

with a  $512 \times 1024$  mesh grid. We choose the proper physical parameters as  $\gamma = 0.5$ ,  $\nu_s = 1.2$ ,  $\epsilon = 5h/(4\sqrt{2}a \tanh(0.9))$ ,  $\Delta t = 0.05h$ ,  $Fr = 0.1$ , and  $Re = 10\,000$ . The density ratio for ternary fluids in this simulation is chosen as  $\rho_1 : \rho_2 : \rho_3 = 8 : 5 : 2$ . The initial conditions for the three components system are chosen as  $\mathcal{F}_8$ . Here, we apply the periodic boundary conditions for velocity field and the homogeneous Neumann boundary conditions for the pressure field. The time evolution of the droplet deformation has been shown in Fig. 10(a). From left to right, the indicated times are  $t = 0.01$ ,  $t = 0.10$ ,  $t = 0.35$ ,  $t = 0.50$ , and  $t = 0.7$ . Figure 10(b) shows the time evolution of the velocity field. The colormap corresponds to the value of velocity, and the arrow represents the direction of flow field. The top droplet ( $\phi_1$ ) falls down, and the bottom droplet ( $\phi_2$ ) moves upward, which is caused by the pressure difference on the interfacial profiles. Under the influence of strong convection, the droplets are stretched and concave inwards. The vortex

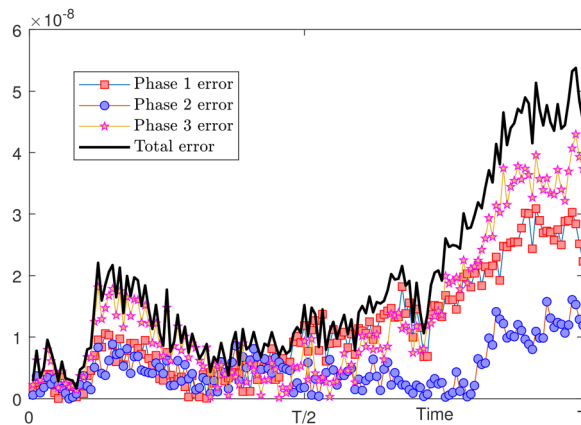


**FIG. 6.** Mass error of the whole multi-component system ( $e_{tot}$ ) and individual component ( $e_{evo}^k$ ).

appears at the tail due to the Rayleigh–Taylor (RT) instability. The droplet will not move since the pressure difference between the two droplets is the same, which corresponds to the physical context.

#### H. Bubble rising under the influence of buoyancy force

In this subsection, we consider the dynamics of a bubble inside other circular bubble embedded in the ambient liquid. Under the influence of buoyancy force, the binary–droplet system is stretched into a flat pack. In order to demonstrate the influence of the density ratio between two bubbles on the results of the dynamical system, we choose different density ratios with the same initial conditions and parameters. In this case, we consider the ternary fluid flows system, which can be initialized as  $\mathcal{F}_9$  in the Appendix. The computational domain is chosen as  $\Omega = [0, 0.5] \times [0, 1]$  with a  $512 \times 1024$  mesh grid. The corresponding physical parameters are chosen as  $\gamma = 1$ ,  $\nu_s = 1$ ,  $\varepsilon = 5h/(4\sqrt{2}a \tanh(0.9))$ ,  $Fr = 0.4$ ,  $Re = 500$ , and  $\Delta t = h^2$ . The density ratios are chosen as  $\rho_1 : \rho_2 : \rho_3 = 1 : 5 : 10$  for Fig. 11(a)

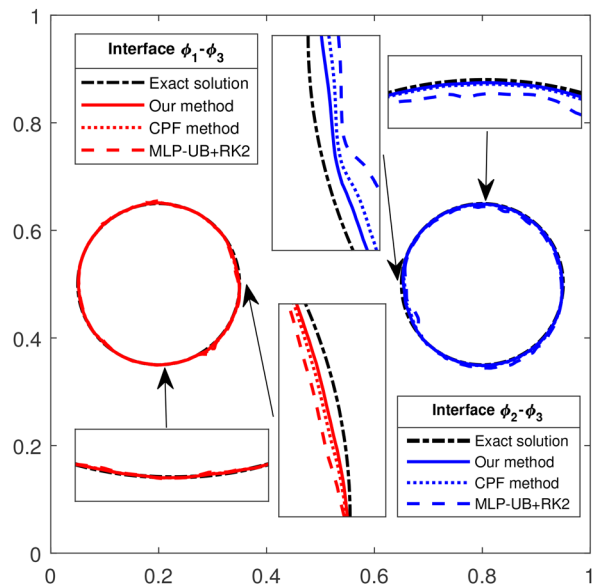


**FIG. 7.** Comparison results obtained by our method, the CPF method in Ref. 54, and the MLP-UB + RK2 method in Ref. 55.

and  $\rho_1 : \rho_2 : \rho_3 = 5 : 1 : 10$  for Fig. 11(b). The colormap demonstrates the shape deformation of the bubbles, and the arrow represents the direction of the flow field. From left to right, the indicated times are  $t = 0.01, 0.10, 0.35, 0.50$ , and  $0.70$ . As shown in Fig. 11, the observed results can be summarized as follows: (i) The bubble with small density is easy to rise under the same background fluids, which corresponds to the physical context. (ii) The bubbles will be stretched even fractured under the surface tension force. (iii) The formed vortex at the tail of the bubble further deepens the deformation. However, the increased contact interfacial profile disperses the surface tension force, which results in no separation between the two bubbles. It is obvious that the proposed model can capture the interface deformation of the multi-component fluid dynamics well.

**TABLE IV.** The comparison results of errors and convergence rates for the Rider–Kothe vortex problem.

Mesh size	1/32	1/64	1/128	1/256
MLP-UB + RK2 errors	...	$2.231 \times 10^{-01}$	$1.242 \times 10^{-01}$	$7.148 \times 10^{-02}$
Rate of convergence	...	...	0.85	0.74
PF errors	$8.203 \times 10^{-02}$	$1.841 \times 10^{-02}$	$5.214 \times 10^{-03}$	$1.584 \times 10^{-03}$
Rate of convergence		2.16	1.82	1.72
LS errors	$6.727 \times 10^{-02}$	$1.469 \times 10^{-02}$	$3.682 \times 10^{-03}$	$7.845 \times 10^{-04}$
Rate of convergence		2.20	1.99	2.23
VOF errors	$3.639 \times 10^{-02}$	$8.964 \times 10^{-03}$	$1.963 \times 10^{-03}$	$3.794 \times 10^{-04}$
Rate of convergence		2.02	2.19	2.37
CPF errors	$3.213 \times 10^{-02}$	$6.174 \times 10^{-03}$	$1.491 \times 10^{-03}$	$3.549 \times 10^{-04}$
Rate of convergence	...	2.38	2.05	2.07
Our errors	$8.472 \times 10^{-03}$	$1.947 \times 10^{-03}$	$5.062 \times 10^{-04}$	$1.239 \times 10^{-04}$
Rate of convergence	...	2.12	1.94	2.03

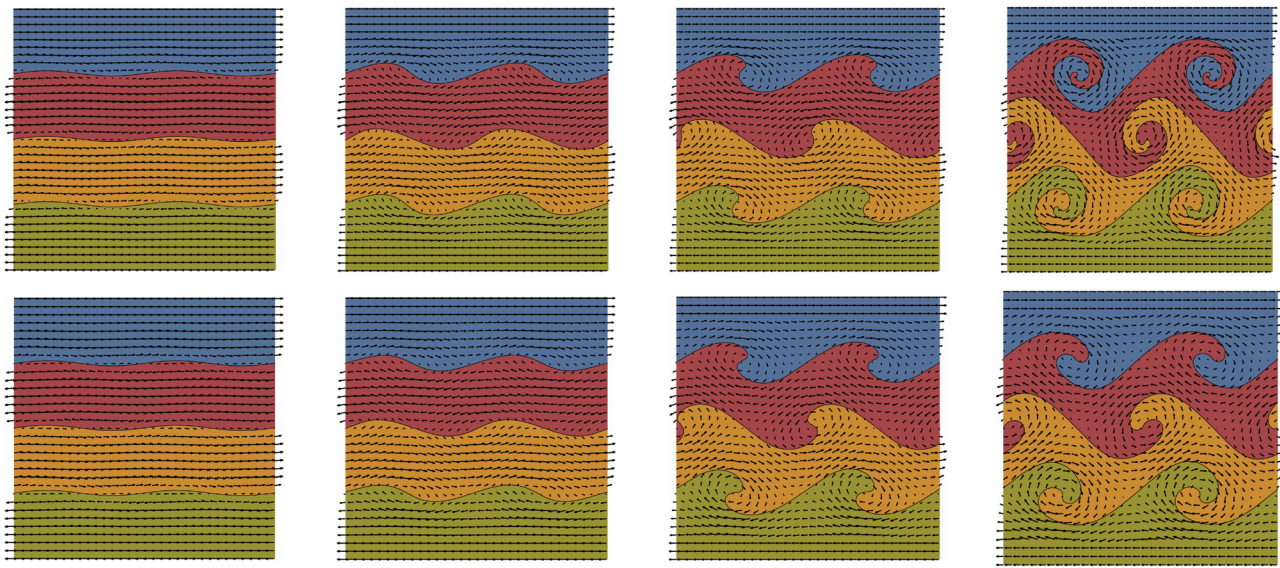


**FIG. 8.** Simulation of KH instability with different Reynolds numbers. The top row is obtained with  $Re = 5000$ , and the bottom row is obtained with  $Re = 500$ . From left to right, the indicated times are  $t = 0, 0.1, 0.3$ , and  $0.5$ .

### I. Dam break flow with convection and slip

In this subsection, we consider the classical dam break problem with flow convection and slip in a ternary fluid flows system. The computational domain is chosen as  $\Omega = [0, 4] \times [0, 2]$  with a  $1024 \times 512$  mesh grid. The corresponding physical parameters are chosen as  $\gamma = 0.5$ ,  $\nu_s = 1.5$ ,  $\varepsilon = 5h/(4\sqrt{2}a \tanh(0.9))$ ,  $Fr = 1$ ,  $Re = 2000$ ,  $\rho_{a1} : \rho_{a2} : \rho_{a3} = 4 : 1 : 2$  and  $\rho_{b1} : \rho_{b2} : \rho_{b3} = 4 : 2 : 1$ , and  $\Delta t = 0.5h^2$ . In order to investigate the influence of convection [12(a)] and slip properties [12(b)] on the dynamic behavior of multi-component interface evolution with different density ratios, we change the layout of multi-component systems, and the initial conditions are chosen as  $\mathcal{F}_{10}$  in the [Appendix](#). The Neumann boundary conditions are applied with no-slip property. We omit the surface tension effect between the ternary fluid system. As can be seen in [Fig. 12\(a\)](#), the greater density difference results a greater pressure difference between

the binary liquids, which is reflected that phase one hits bottom faster than phase three on the dynamic behavior points of view. The two phases collide at the bottom of the box, which converts the horizontal momentum to vertical momentum. The fluid at the bottom is pushed upward and forms a spray-like dynamic pattern. As a result, a water jump with complicated interface configurations has been captured by the proposed multi-component system. As can be seen in [Fig. 12\(b\)](#), the two fluids flow and slip horizontally during the descent processing. Since phase one is denser than phase three, phase one gets more gravitational potential energy than phase three in the initial state. According to the law of conservation of energy, phase one gets more kinetic energy in the process of dam break. We have applied a small amplitude perturbed interface between the ternary fluids system at the initial state, and thus, the KH instability occurs on the interfacial transition while the velocity difference is sufficiently large. It is obvious

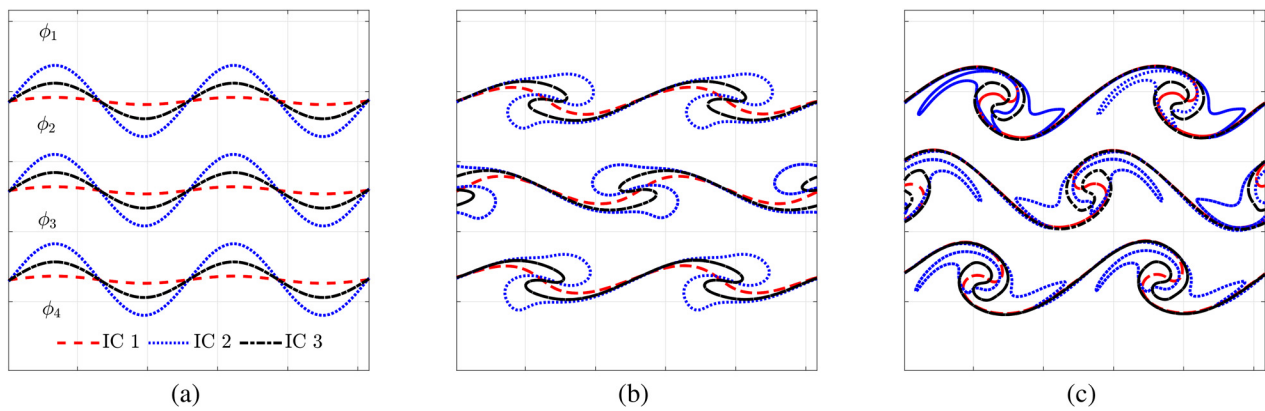


**FIG. 9.** Simulation of KH instability with different initial conditions. From (a)–(c), the indicated times are  $t = 0, 0.25$ , and  $0.5$ , respectively.

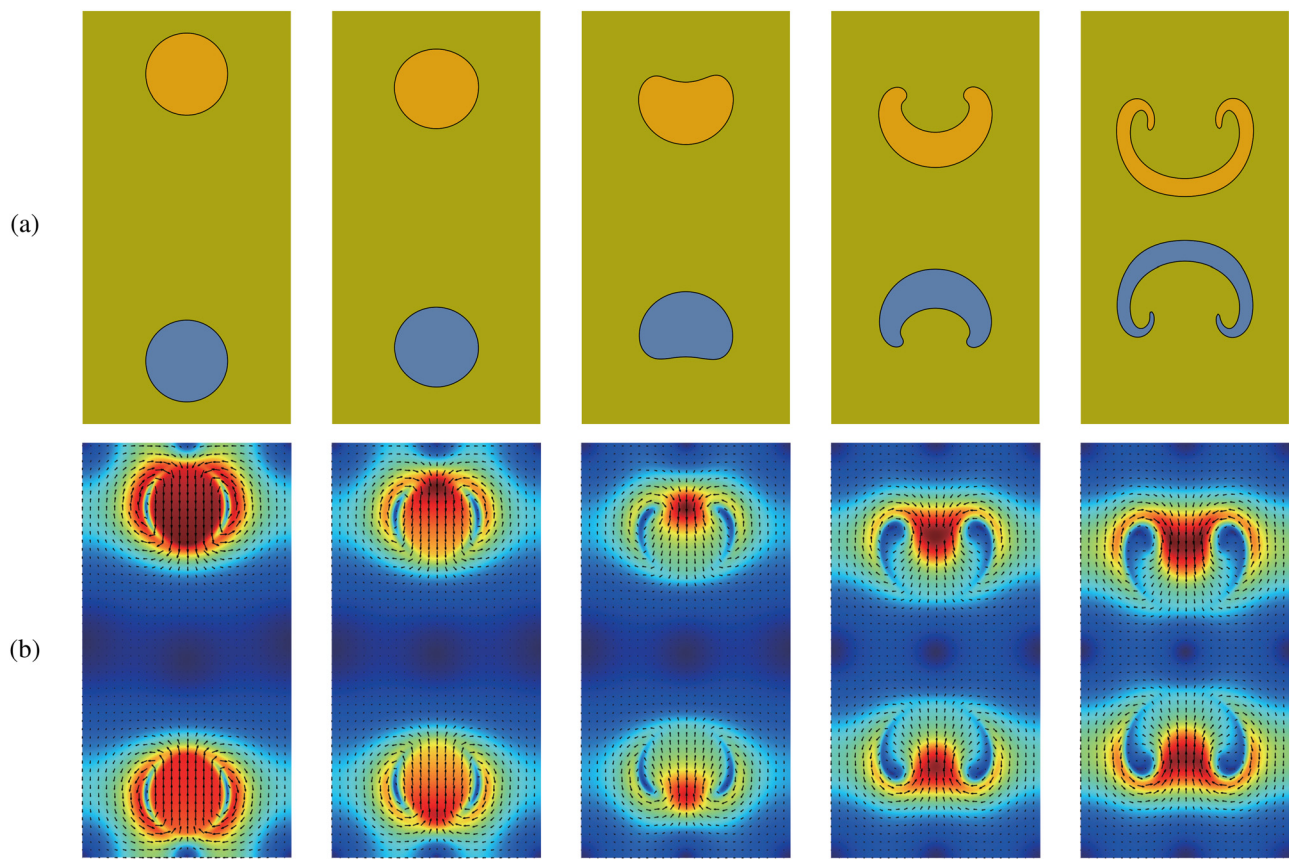


**FIG. 10.** The dynamical behaviors of the buoyancy-driven bubble. (a) and (b) Evolutions of phase separations and the velocity field, respectively. The colormap corresponds to the value of velocity, and the arrow represents the direction of the flow field. From left to right, the indicated times are  $t = 0.01, 0.10, 0.35, 0.50$ , and  $0.70$ .

that the dam break problem with flow convection and slip can be tracked well, which corresponds with the physical context. As shown in Figs. 13(a) and 13(b), we demonstrate the velocity at the final time of Figs. 12(a) and 12(b). As can be seen in Fig. 13, we compute the average divergence of the multi-component system and list the values of the average divergence at various specific moments of the dynamic evolution of Fig. 12. It can be seen that the average divergence of the velocity approximately equals zero, which implies that the mass is conserved throughout the computation.

### J. Investigation of Rayleigh–Taylor instability

In this subsection, we consider the investigation of Rayleigh–Taylor (RT) instability with no surface tension. The RT instability phenomenon occurs at the interface between two fluids of different densities when a small disturbance occurs. In order to investigate the performance of the proposed method for tracking the dynamic interfacial profile in the multi-component system, we consider the RT instability of four components fluid flows with long time simulation, which can be used for the prediction of the interfacial transition from laminar to turbulent flow. The computational domain is chosen as  $\Omega = [0, 1] \times [0, 4]$  with a  $256 \times 1024$  mesh grid. The corresponding physical parameters are chosen as

$\gamma = 0.5$ ,  $\nu_s = 1.2$ ,  $\varepsilon = 5h/(4\sqrt{2}a \tanh(0.9))$ ,  $Fr = 0.4$ ,  $Re = 5000$ ,  $\rho_1 : \rho_2 : \rho_3 : \rho_4 = 4 : 3 : 2 : 1$ , and  $\Delta t = h^2$ . The initial conditions are chosen as  $\mathcal{F}_{11}$  in the Appendix. The zero Neumann boundary conditions are applied for  $\phi$  and the homogeneous Neumann boundary conditions for  $\mathbf{u}$  and  $p$ . As can be seen from Fig. 14, the time evolution of the interface capturing for the four-component system has been demonstrated at the indicated times  $t = 0.0, 0.4, 0.8, 1.2, 1.6$ , and  $2.0$ . The amplitude of the initial perturbation grows up under the influence of the pressure difference ( $t = 0.4$ ). The heavier fluids fall to form a spike interface, while the secondary instability is triggered at the two sides of the tail of the lighter fluid ( $t = 1.2$ ). The tertiary instability occurred when there is no barrier between the different fluids, i.e., the different phases are affected by turbulence and collide with each other ( $t = 2.0$ ). It is obvious that the proposed method works well for capturing more details and adapt to dramatical shocks with the multi-component system.

### K. Extension to complicated physical process with long time simulation

In this subsection, we coupled several complex physical processes together, such as bubble rising, RT instability, KH instability, to investigate the stability and applicability of the proposed method with a

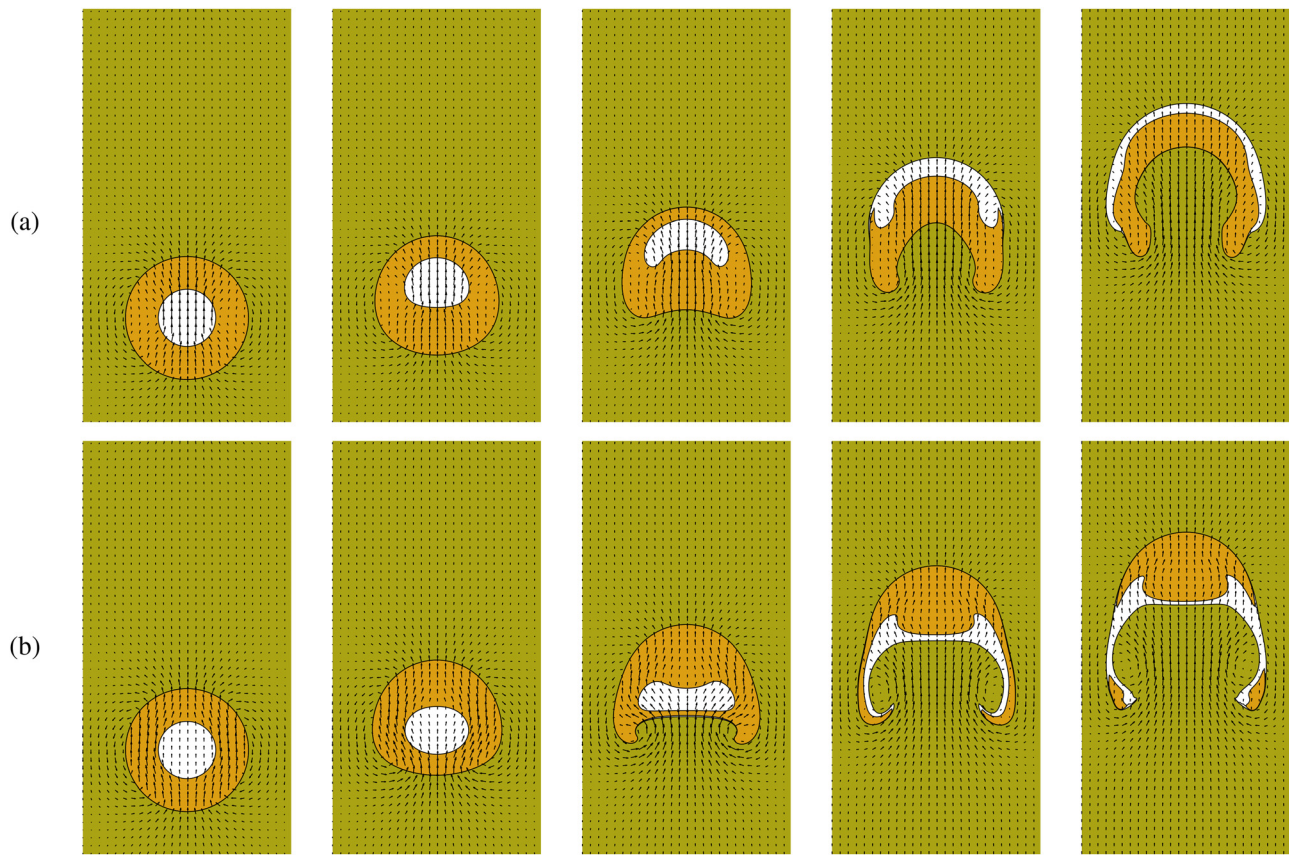


**FIG. 11.** The dynamical behaviors of the buoyancy-driven bubble. (a) and (b) Evolutions of phase separations and temperature field coupled the velocity field, respectively. From left to right, the indicated times are  $t = 0.01, 0.10, 0.35, 0.50$ , and  $0.70$ .

long time simulation. The computational domain is chosen as  $\Omega = [0, 2] \times [0, 4]$  with a  $512 \times 1024$  mesh grid. The corresponding physical parameters are chosen as  $\gamma = 1$ ,  $\nu_s = 1$ ,  $\rho_1 : \rho_2 : \rho_3 = 1 : 4 : 2$ ,  $\varepsilon = 5h/(4\sqrt{2}a \tanh(0.9))$ ,  $Fr = 0.5$ ,  $Re = 1000$ , and  $\Delta t = 5h^2$ . As can

be seen from Fig. 15, we consider a dynamic process in which the bottom axisymmetric bubble rises continuously under the influence of pressure gradient (caused by density difference), and the top fluids falls continuously under the influence of gravity. We consider the hybrid



**FIG. 12.** The evolution of the interface tracking with dam break problem at  $t = 0.0$ ,  $t = 1.0$ , and  $t = 2.0$ . (a) The flow convection of ternary fluids with the density ratio  $\rho_{a1} : \rho_{a2} : \rho_{a3} = 4 : 1 : 2$ . (b) The flow slip of ternary fluids with the density ratio  $\rho_{b1} : \rho_{b2} : \rho_{b3} = 4 : 2 : 1$ .

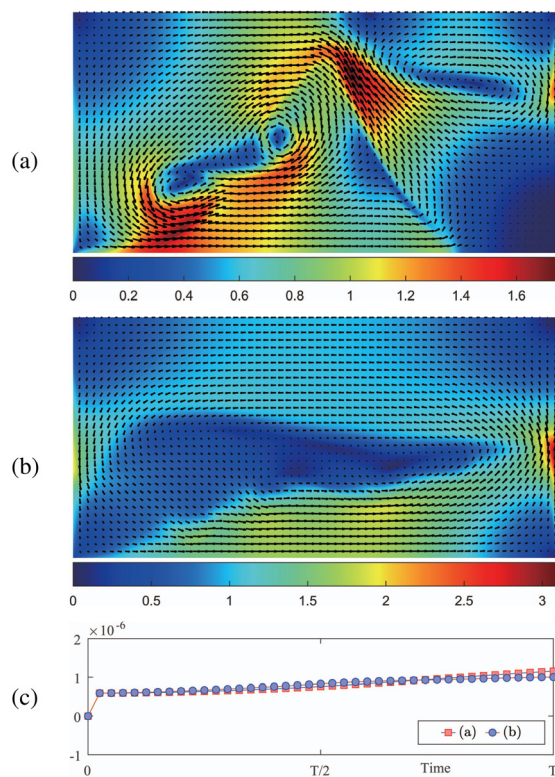


**FIG. 13.** (a) and (b) The velocity at the final time of Figs. 12(a) and 12(b), respectively. (c) The average divergence for (a) and (b) at various moments. The color-map corresponds to the value of velocity, and the arrow represents the direction of flow field.

system is consisted of three components, which can be initialized as  $\mathcal{F}_{12}$  in the Appendix.

The bubble rise upward driven by the buoyancy effect. From Figs. 15(a) and 15(b), the bottom part of the rising bubble moves faster, which causes the bubbles to deform from circle to oval. As can be seen from Figs. 15(c) and 15(d), when the bubble passes through the interface between the binary phases for the first time, the left and right sides of the bubble squeeze inward under the influence of surface tension, resulting in the deformation of the bubble. Before the second transition, the bubble is compressed into a flattened shape between phase two and phase three. From Figs. 15(e)–15(g), the bubble merges with the gas at the top of the box (phase one), while the interfacial profile between phase one and phase two breaks up. The mushroom-like shape interface has been formed with phase two falling under gravity and phase three rising under buoyancy. Blocked by phase one, phase three exhibits the finger shape caused by RT instability, until phase three and phase two switch positions under the influence of density gradient. The satellite droplets trapped between the phase one and the phase three surface form the small bubbles at the underside of the pool of phase one. From Figs. 15(h)–15(j), after the reconstruction of the interface, local turbulence has appeared to balance the extrusion deformation between different phases. Eventually, the total momentum has disappeared, and the static equilibrium has been realized in the multi-component system. This long time simulation of the ternary fluids system with complex behavior well confirms that our method has high accuracy and high applicability.

## V. CONCLUSIONS

In this paper, we proposed a consistent system coupled the conservative AC equation and the incompressible NS equation for the

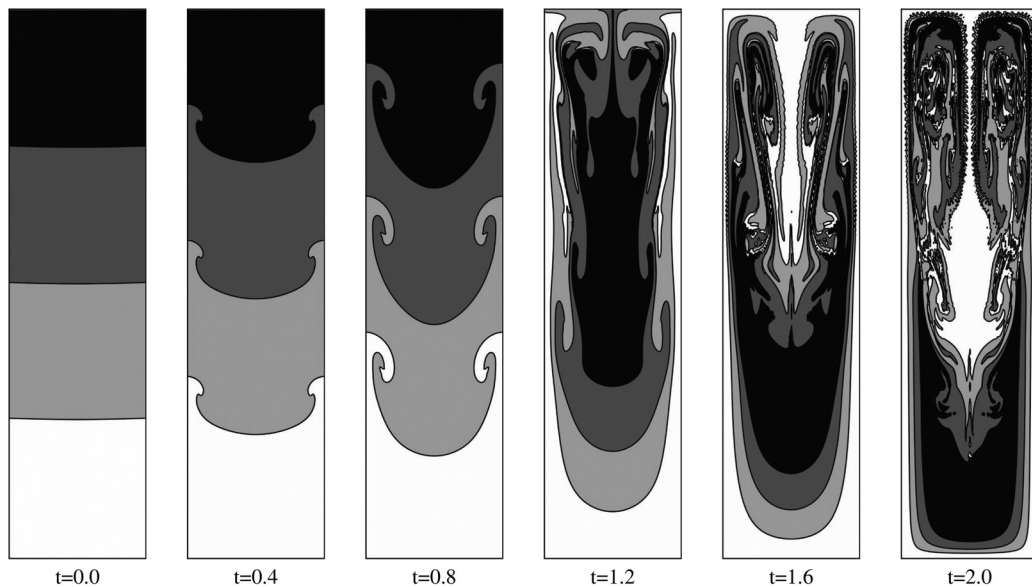


**FIG. 14.** Time evolution of the interface capturing in the four-phase Rayleigh–Taylor instability problem at the indicated times:  $t = 0.0$ ,  $t = 0.4$ ,  $t = 0.8$ ,  $t = 1.2$ ,  $t = 1.6$ ,  $t = 2.0$ . The density ratio is chosen as  $\rho_1 : \rho_2 : \rho_3 : \rho_4 = 4 : 3 : 2 : 1$ .

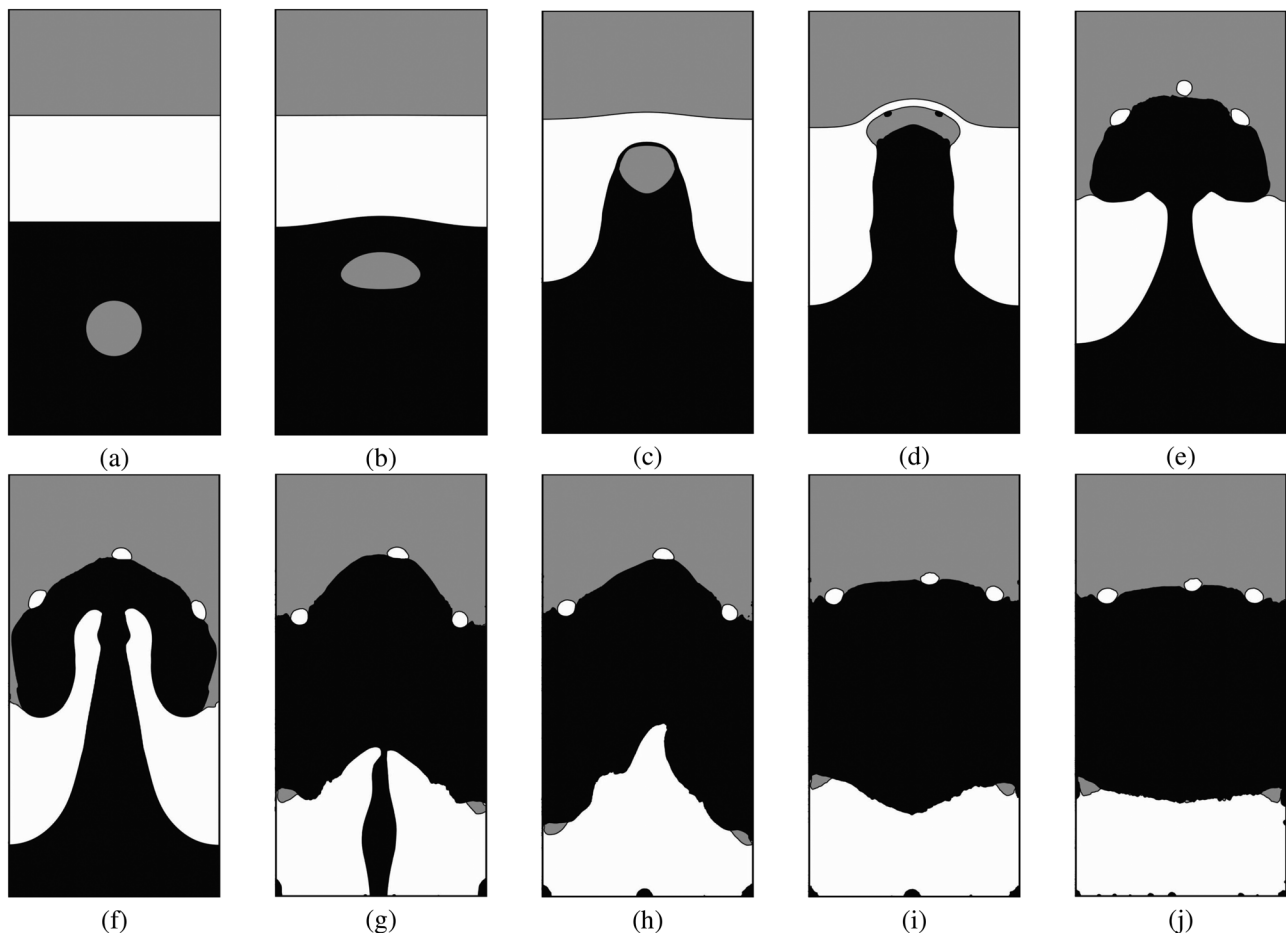


**FIG. 15.** The dynamical behaviors of the tracking interfaces under the three-component flow framework. The density ratio for the investigated system is  $\rho_1 : \rho_2 : \rho_3 = 1 : 4 : 2$ . From (a)–(j), the indicated times are  $t = 0.0, 0.1, 0.3, 0.5, 0.7, 0.9, 1.5, 2.0, 2.50$ , and 5.0, respectively.

N-component immiscible fluids system based on the phase-field model. We used the transition region with finite thickness to represent the interfaces between immiscible components with the continuous phase field. The surface tension effects between any combination of interfaces were represented with the continuous surface tension force in the N-component system, which is not limited by the number of components. The surface tension force per unit volume that acts in a neighborhood of the interface was well examined in the transition region. A hyperbolic Dirac function was used to smooth the deformation of interfaces between different phases. The proposed conservative model can track the interface with large deformation in divergence-free velocity fields. Under the guidance of the nonlinear preprocessing operation based on the level-set method, the improved phase-field-based method has been coupled with the local artificial viscosity stabilization to modify the computation of the discrete normal vector, which caused the spurious oscillations. We utilized the third-order Runge-Kutta time discretization and second-order spatial discretization. The spurious oscillations caused by discontinuous and steep gradient for capturing the shocks and sharp interfaces have been eliminated by applying the third-order WENO method for the

advection term. The multigrid method has been applied for the computation of the discrete system at implicit time steps. Various representative computational tests showed the applicability, and several benchmark cases demonstrated the high accuracy of our proposed method.

In the future work, we will consider the hybrid system with variable densities driven by the quasi-compressible fluids flow. Furthermore, we will consider the spurious oscillations caused by discontinuous and steep gradients for capturing the shocks and sharp interfaces under the compressible system.

## ACKNOWLEDGMENTS

Y. B. Li is supported by the National Natural Science Foundation of China (No. 12271430). Q. Xia is supported by the Fundamental Research Funds for the Central Universities, China (No. XYZ022022005). J. Yang is supported by the National Natural Science Foundation of China (No. 12201657) and the China Postdoctoral Science Foundation (No. 2022M713639). The authors would like to thank the reviewers for their constructive and helpful comments regarding the revision of this article.

**AUTHOR DECLARATIONS****Conflict of Interest**

The authors have no conflicts to disclose.

**Author Contributions**

**Qing Xia:** Methodology (equal); Project administration (equal); Resources (equal); Software (equal); Supervision (equal); Validation (equal); Visualization (equal); Writing – original draft (equal); Writing – review & editing (equal). **Junxiang Yang:** Methodology (equal); Project administration (equal); Writing – review & editing (equal). **Yibao Li:** Formal analysis (equal); Project administration (equal); Resources (equal); Supervision (equal).

**DATA AVAILABILITY**

The data that support the findings of this study are available from the corresponding author upon reasonable request.

**APPENDIX: INITIAL CONDITIONS FOR NUMERICAL TESTS**

$\mathcal{F}_1$ : Initial condition for convergence test

$$\phi_1(x, y, 0) = 0.5 + 0.5 \tanh\left(\frac{((x - 0.5)^2 + (y - 0.5)^2 - 0.25)}{\sqrt{5}\varepsilon}\right), \quad (\text{A1a})$$

$$\phi_2(x, y, 0) = 1 - \phi_1(x, y, 0), \quad (\text{A1b})$$

$$u(x, y, 0) = \cos(x) \cos(y), \quad v(x, y, 0) = \sin(x) \cos(y), \quad (\text{A1c})$$

$$p(x, y, 0) = -\cos(x) \sin(y). \quad (\text{A1d})$$

$\mathcal{F}_2$ : Initial condition for parameter analysis

$$\phi_1(x, y, 0) = \frac{1}{2} \left( 1 + \tanh\left(\frac{\sqrt{(x - 0.5)^2 + (y - 0.5)^2 - 0.1}}{2\sqrt{2}\varepsilon}\right) \right), \quad (\text{A2a})$$

$$\phi_3(x, y, 0) = \frac{1}{2} \left( 1 + \tanh\left(\frac{\sqrt{(x - 0.5)^2 + (y - 0.5)^2 - 0.2}}{2\sqrt{2}\varepsilon}\right) \right), \quad (\text{A2b})$$

$$\phi_2(x, y, 0) = 1 - \phi_1(x, y, 0) - \phi_3(x, y, 0), \quad (\text{A2c})$$

$$u(x, y, 0) = 0, \quad v(x, y, 0) = 0, \quad p(x, y, 0) = 0. \quad (\text{A2d})$$

$\mathcal{F}_3$ : Initial condition for capillary filling test

$$\phi_1(x, y, 0) = 0.5 - 0.5 \tanh\left((x - 1 - 0.01 \sin(4\pi x))/(2\sqrt{2}\varepsilon)\right), \quad (\text{A3a})$$

$$\phi_3(x, y, 0) = 0.5 + 0.5 \tanh\left((x - 3 - 0.01 \sin(4\pi x))/(2\sqrt{2}\varepsilon)\right), \quad (\text{A3b})$$

$$\phi_2(x, y, 0) = 1 - \phi_1(x, y, 0) - \phi_3(x, y, 0), \quad (\text{A3c})$$

$$u(x, y, 0) = 0, \quad v(x, y, 0) = 0, \quad p(x, y, 0) = 0. \quad (\text{A3d})$$

$\mathcal{F}_4$ : Initial condition for rotation under the background velocity field in Fig. 4

$$\phi_1(x, y, 0) = 0.5 - 0.5 \tanh\left(\frac{(|x - 0.5| + (y - 0.25)^2 - 0.03)}{\sqrt{5}\varepsilon}\right), \quad (\text{A4a})$$

$$\phi_2(x, y, 0) = 0.5 - 0.5 \tanh\left(\frac{(|x - 0.5| + (y - 0.75)^2 - 0.03)}{\sqrt{5}\varepsilon}\right), \quad (\text{A4b})$$

$$\phi_3(x, y, 0) = 0.5 - 0.5 \tanh\left(\frac{((x - 0.75)^2 + |y - 0.5| - 0.03)}{\sqrt{5}\varepsilon}\right), \quad (\text{A4c})$$

$$\phi_4(x, y, 0) = 0.5 - 0.5 \tanh\left(\frac{((x - 0.25)^2 + |y - 0.5| - 0.03)}{\sqrt{5}\varepsilon}\right), \quad (\text{A4d})$$

$$\phi_5(x, y, 0) = 1 - \phi_1(x, y, 0) - \phi_2(x, y, 0) - \phi_3(x, y, 0) - \phi_4(x, y, 0), \quad (\text{A4e})$$

$$u(x, y, 0) = 16(y - 0.5), \quad v(x, y, 0) = -16(x - 0.5), \quad (\text{A4f})$$

$$p(x, y, 0) = 0. \quad (\text{A4g})$$

$\mathcal{F}_5$ : Initial condition for rotation under the background velocity field in Fig. 5

$$\phi_1(x, y, 0) = 0.5 + 0.5 \tanh((|x - 0.75| + |x - 0.45| + |y - 0.50| + |y - 0.80| - 0.6)/(2\sqrt{2}\varepsilon)), \quad (\text{A5a})$$

$$\phi_2(x, y, 0) = 0.5 + 0.5 \tanh((|x - 0.75| + |x - 0.45| + |y - 0.50| + |y - 0.20| - 0.6)/(2\sqrt{2}\varepsilon)), \quad (\text{A5b})$$

$$\phi_3(x, y, 0) = 0.5 + 0.5 \tanh((|x - 0.15| + |x - 0.45| + |y - 0.35| + |y - 0.65| - 0.6)/(2\sqrt{2}\varepsilon)), \quad (\text{A5c})$$

$$\phi_4(x, y, 0) = 1 - c_1(x, y, 0) - c_2(x, y, 0) - c_3(x, y, 0), \quad (\text{A5d})$$

$$u(x, y, 0) = -16(y - 0.5), \quad v(x, y, 0) = 16(x - 0.5), \quad (\text{A5e})$$

$$p(x, y, 0) = 0. \quad (\text{A5f})$$

$\mathcal{F}_6$ : Initial condition for the investigation of Rider–Kothe vortex

$$u = -\sin(\pi y) \cos(\pi y) \sin(\pi x)^2 \cos\left(\pi \frac{t}{T}\right), \quad (\text{A6a})$$

$$v = \sin(\pi x) \cos(\pi x) \sin(\pi y)^2 \cos\left(\pi \frac{t}{T}\right), \quad (\text{A6b})$$

$$\phi_1(x, y, 0) = 0.5$$

$$+ 0.5 \tanh\left(\frac{((x - 0.25)^2 + (y - 0.5)^2 - 0.15)}{\sqrt{5}\varepsilon}\right), \quad (\text{A6c})$$

$$\phi_2(x, y, 0) = 0.5 + 0.5 \tanh\left(\frac{((x - 0.75)^2 + (y - 0.5)^2 - 0.15)}{\sqrt{5}\varepsilon}\right), \quad (\text{A6d})$$

$$\phi_3(x, y, 0) = 1 - \phi_1(x, y, 0) - \phi_2(x, y, 0). \quad (\text{A6e})$$

$\mathcal{F}_7$ : Initial condition for the simulation of perturbation with Kelvin–Helmholtz instability

$$u(x, y, 0)$$

$$\begin{aligned} &= \tanh\left(\frac{(y - 0.25 - 0.02 \sin(4\pi x))}{(0.02\sqrt{2})}\right) \\ &- \tanh\left(\frac{(y - 0.50 - 0.02 \sin(4\pi x))}{(0.02\sqrt{2})}\right) \\ &+ \tanh\left(\frac{(y - 0.75 - 0.02 \sin(4\pi x))}{(0.02\sqrt{2})}\right), \end{aligned} \quad (\text{A7a})$$

$$v(x, y, 0) = 0, \quad p(x, y, 0) = 0, \quad (\text{A7b})$$

$$\phi_1(x, y, 0) = 0.5 + 0.5 \tanh\left(\frac{(y - 0.75 - 0.01 \sin(4\pi x))}{(2\sqrt{2}\varepsilon)}\right), \quad (\text{A7c})$$

$$\begin{aligned} \phi_2(x, y, 0) &= 0.5 \tanh\left(\frac{(y - 0.5 - 0.01 \sin(4\pi x))}{(2\sqrt{2}\varepsilon)}\right) \\ &- 0.5 \tanh\left(\frac{(y - 0.75 - 0.01 \sin(4\pi x))}{(2\sqrt{2}\varepsilon)}\right), \end{aligned} \quad (\text{A7d})$$

$$\begin{aligned} \phi_3(x, y, 0) &= 0.5 \tanh\left(\frac{(y - 0.25 - 0.01 \sin(4\pi x))}{(2\sqrt{2}\varepsilon)}\right) \\ &- 0.5 \tanh\left(\frac{(y - 0.5 - 0.01 \sin(4\pi x))}{(2\sqrt{2}\varepsilon)}\right), \end{aligned} \quad (\text{A7e})$$

$$\phi_4(x, y, 0) = 1 - \phi_1(x, y, 0) - \phi_2(x, y, 0) - \phi_3(x, y, 0). \quad (\text{A7f})$$

$\mathcal{F}_8$ : Initial condition for the droplet hedging under the influence of gravity

$$u(x, y, 0) = v(x, y, 0) = 0, \quad p(x, y, 0) = 0, \quad (\text{A8a})$$

$$\phi_1(x, y, 0) = 0.5 + 0.5 \tanh\left(\frac{\left(0.1 - \sqrt{(x - 0.25)^2 + (y - 0.85)^2}\right)}{(2\sqrt{2}\varepsilon)}\right), \quad (\text{A8b})$$

$$\phi_3(x, y, 0) = 0.5 + 0.5 \tanh\left(\frac{\left(0.1 - \sqrt{(x - 0.25)^2 + (y - 0.15)^2}\right)}{(2\sqrt{2}\varepsilon)}\right), \quad (\text{A8c})$$

$$\phi_2(x, y, 0) = 1 - \phi_1(x, y, z, 0) - \phi_3(x, y, z, 0). \quad (\text{A8d})$$

$\mathcal{F}_9$ : Initial condition for the bubble rising under the influence of buoyancy force

$$u(x, y, 0) = v(x, y, 0) = 0, \quad p(x, y, 0) = 0, \quad (\text{A9a})$$

$$\phi_1(x, y, 0) = \frac{1}{2} \left( 1 + \tanh(0.075 - \sqrt{(x - 0.25)^2 + (y - 0.25)^2}) \right) / (2\sqrt{2}\varepsilon), \quad (\text{A9b})$$

$$\phi_2(x, y, 0) = \frac{1}{2} \tanh(0.15 \sqrt{(x - 0.25)^2 + (y - 0.25)^2}) / (2\sqrt{2}\varepsilon) \quad (\text{A9c})$$

$$\begin{aligned} &- \frac{1}{2} \tanh\left(0.075 - \sqrt{(x - 0.25)^2 + (y - 0.25)^2}\right) / (2\sqrt{2}\varepsilon) \\ &(2\sqrt{2}\varepsilon), \end{aligned} \quad (\text{A9d})$$

$$\phi_3(x, y, 0) = 1 - \phi_1(x, y, 0) - \phi_2(x, y, 0). \quad (\text{A9e})$$

$\mathcal{F}_{10}$ : Initial condition for dam break flow with convection and slip

$$u(x, y, 0) = v(x, y, 0) = 0, \quad p(x, y, 0) = 0, \quad (\text{A10a})$$

$$\phi_{a1}(x, y, 0) = 0.5 - 0.5 \tanh\left(\frac{(x - 1 - 0.01 \sin(4\pi x))}{(2\sqrt{2}\varepsilon)}\right), \quad (\text{A10b})$$

$$\phi_{b1}(x, y, 0) = \phi_{a1}(x, y, 0), \quad (\text{A10c})$$

$$\begin{aligned} \phi_{a2}(x, y, 0) &= 0.5 - 0.5 \tanh\left(\frac{(x - 2 - 0.01 \sin(4\pi x))}{(2\sqrt{2}\varepsilon)}\right) \\ &- \phi_{a1}(x, y, 0), \end{aligned} \quad (\text{A10d})$$

$$\phi_{b2}(x, y, 0) = 0.5 + 0.5 \tanh\left(\frac{(x - 3 - 0.01 \sin(4\pi x))}{(2\sqrt{2}\varepsilon)}\right), \quad (\text{A10e})$$

$$\phi_{a3}(x, y, 0) = 1 - \phi_{a1}(x, y, 0) - \phi_{a2}(x, y, 0), \quad (\text{A10f})$$

$$\phi_{b3}(x, y, 0) = 1 - \phi_{b1}(x, y, 0) - \phi_{b2}(x, y, 0). \quad (\text{A10g})$$

$\mathcal{F}_{11}$ : Initial condition for investigation of Rayleigh–Taylor instability

$$u(x, y, 0) = v(x, y, 0) = 0, \quad p(x, y, 0) = 0, \quad (\text{A11a})$$

$$\phi_1(x, y, 0) = 0.5 + 0.5 \tanh\left(\frac{(y - 3 - 0.01 \sin(\pi(x + 1)))}{(2\sqrt{2}\varepsilon)}\right) \quad (\text{A11b})$$

$$\begin{aligned} \phi_2(x, y, 0) &= 0.5 - \phi_1(x, y, 0) \\ &+ 0.5 \tanh\left(\frac{(y - 2 - 0.01 \sin(\pi(x + 1)))}{(2\sqrt{2}\varepsilon)}\right) \end{aligned} \quad (\text{A11c})$$

$$\begin{aligned} \phi_3(x, y, 0) &= 0.5 \tanh\left(\frac{(y - 1 - 0.01 \sin(\pi(x + 1)))}{(2\sqrt{2}\varepsilon)}\right) \\ &- 0.5 \tanh\left(\frac{(y - 2 - 0.01 \sin(\pi(x + 1)))}{(2\sqrt{2}\varepsilon)}\right), \end{aligned} \quad (\text{A11d})$$

$$\phi_4(x, y, 0) = 1 - \phi_1(x, y, 0) - \phi_2(x, y, 0) - \phi_3(x, y, 0). \quad (\text{A11e})$$

$\mathcal{F}_{12}$ : Initial condition for extension to the complicated physical process with long time simulation

$$u(x, y, 0) = v(x, y, 0) = 0, \quad p(x, y, 0) = 0, \quad (\text{A12a})$$

$$\begin{aligned} \phi_1(x, y, 0) &= 1 - 0.5 \tanh\left(\frac{(y - 1 - 0.01 \sin(\pi x))}{(2\sqrt{2}\varepsilon)}\right) \\ &+ 0.5 \tanh\left(20 - \sqrt{(x - 1)^2 + (y - 3)^2} / (2\sqrt{2}\varepsilon)\right), \end{aligned} \quad (\text{A12b})$$

$$\begin{aligned} \phi_2(x, y, 0) &= -0.5 \tanh\left(\frac{(y - 2 - 0.01 \sin(\pi x))}{(2\sqrt{2}\varepsilon)}\right) \\ &+ 0.5 \tanh\left(\frac{(y - 1 - 0.01 \sin(\pi x))}{(2\sqrt{2}\varepsilon)}\right), \end{aligned} \quad (\text{A12c})$$

$$\phi_3(x, y, 0) = 1 - \phi_1(x, y, 0) - \phi_2(x, y, 0). \quad (\text{A12d})$$

## REFERENCES

<sup>1</sup>Z. Yang, H. Fang, K. Jin, J. He, W. Ge, and W. Yan, “Modeling of microstructure evolution coupled with molten pool oscillation during electron beam welding of an Al–Cu alloy,” *Int. J. Heat Mass Transfer* **189**, 122735 (2022).

<sup>2</sup>M. H. Dao and J. Lou, “Simulations of laser assisted additive manufacturing by smoothed particle hydrodynamics,” *Comput. Methods Appl. Mech. Eng.* **373**, 113491 (2021).

- <sup>3</sup>E. Facca, F. Cardin, and M. Putti, "Branching structures emerging from a continuous optimal transport model," *J. Comput. Phys.* **447**, 110700 (2021).
- <sup>4</sup>B. Li and X. Li, "A cross-diffusive evolution system arising from biological transport networks," *Commun. Nonlinear Sci. Numer. Simul.* **92**, 105465 (2021).
- <sup>5</sup>Q. Xia, Q. Yu, and Y. Li, "A second-order accurate, unconditionally energy stable numerical scheme for binary fluid flows on arbitrarily curved surfaces," *Comput. Methods Appl. Mech. Eng.* **384**, 113987 (2021).
- <sup>6</sup>Y. Li, R. Liu, Q. Xia, C. He, and Z. Li, "First- and second-order unconditionally stable direct discretization methods for multi-component Cahn-Hilliard system on surfaces," *J. Comput. Appl. Math.* **401**, 113778 (2022).
- <sup>7</sup>T. Uchida and Y. Ohya, "Numerical simulation of atmospheric flow over complex terrain," *J. Wind Eng. Ind. Aerodyn.* **81**, 283–293 (1999).
- <sup>8</sup>M. Aggul and A. E. Labovsky, "Approximate deconvolution models for a fluid-fluid interaction problem with high Reynolds numbers," *Comput. Math. Appl.* **117**, 113–126 (2022).
- <sup>9</sup>J. Al-Salami, M. M. Kamra, and C. Hu, "A high order flux reconstruction interface capturing method with a phase field preconditioning procedure," *J. Comput. Phys.* **438**, 110376 (2021).
- <sup>10</sup>J. Kim, "A generalized continuous surface tension force formulation for phase-field models for multi-component immiscible fluid flows," *Comput. Methods Appl. Mech. Eng.* **198**, 3105–3112 (2009).
- <sup>11</sup>Y. Li, Q. Xia, S. Yoon, C. Lee, B. Lu, and J. Kim, "Simple and efficient volume merging method for triply periodic minimal structures," *Comput. Phys. Commun.* **264**, 107956 (2021).
- <sup>12</sup>J. A. Mcfarland, W. J. Black, J. Dahal, and B. E. Morgan, "Computational study of the shock driven instability of a multiphase particle-gas system," *Phys. Fluids* **28**, 024105 (2016).
- <sup>13</sup>T. Zhang, J. Wu, and X. Lin, "An interface-compressed diffuse interface method and its application for multiphase flows," *Phys. Fluids* **31**, 122102 (2019).
- <sup>14</sup>K. Kleefsman, G. Fekken, A. Veldman, B. Iwanowski, and B. Buchner, "A volume-of-fluid based simulation method for wave impact problems," *J. Comput. Phys.* **206**, 363–393 (2005).
- <sup>15</sup>M. M. Kamra, N. Mohd, C. Liu, M. Sueyoshi, and C. Hu, "Numerical and experimental investigation of three-dimensionality in the dam-break flow against a vertical wall," *J. Hydraul.* **30**, 682–693 (2018).
- <sup>16</sup>K. J. Petersen and J. R. Brinkerhoff, "On the lattice Boltzmann method and its application to turbulent, multiphase flow of various fluids including cryogens: A review," *Phys. Fluids* **33**, 041302 (2021).
- <sup>17</sup>S. Matsushita and T. Aoki, "A weakly compressible scheme with a diffuse-interface method for low Mach number two-phase flows," *J. Comput. Phys.* **376**, 838–862 (2019).
- <sup>18</sup>Q. Xia, J. Kim, B. Xia, and Y. Li, "An unconditionally energy stable method for binary incompressible heat conductive fluids based on the phase-field model," *Comput. Math. Appl.* **123**, 26–39 (2022).
- <sup>19</sup>W. Yang, M. Jia, K. Sun, and T. Wang, "Influence of density ratio on the secondary atomization of liquid droplets under highly unstable conditions," *Fuel* **174**, 25–35 (2016).
- <sup>20</sup>Y. Pei, S. Som, E. Pomraning, P. K. Senecal, S. A. Skeen, J. Manin, and L. M. Pickett, "Large eddy simulation of a reacting spray flame with multiple realizations under compression ignition engine conditions," *Combust. Flame* **162**, 4442–4455 (2015).
- <sup>21</sup>E. Olsson and G. Kreiss, "A conservative level set method for two phase flow," *J. Comput. Phys.* **210**, 225–246 (2005).
- <sup>22</sup>N. Shervani-Tabar and O. V. Vasilyev, "Stabilized conservative level set method," *J. Comput. Phys.* **375**, 1033–1044 (2018).
- <sup>23</sup>R. P. Fedkiw, T. Aslam, and S. Xu, "The ghost fluid method for deflagration and detonation discontinuities," *J. Comput. Phys.* **154**, 393–427 (1999).
- <sup>24</sup>O. Desjardins, V. Moureau, and H. Pitsch, "An accurate conservative level set/ghost fluid method for simulating turbulent atomization," *J. Comput. Phys.* **227**, 8395–8416 (2008).
- <sup>25</sup>J. Kim and J. Lowengrub, "Phase field modeling and simulation of three-phase flows," *Interfaces Free Boundaries* **7**, 435–466 (2005).
- <sup>26</sup>S. Dong, "An efficient algorithm for incompressible N-phase flows," *J. Comput. Phys.* **276**, 691–728 (2014).
- <sup>27</sup>S. Dong, "Multiphase flows of N immiscible incompressible fluids: A reduction-consistent and thermodynamically-consistent formulation and associated algorithm," *J. Comput. Phys.* **361**, 1–49 (2018).
- <sup>28</sup>H. Y. Li, Y. F. Yap, J. Lou, and Z. Shang, "Numerical modeling of three-fluid flow using the level-set method," *Chem. Eng. Sci.* **126**, 224–236 (2015).
- <sup>29</sup>A. A. Howard and A. M. Tartakovsky, "A conservative level set method for N-phase flows with a free-energy-based surface tension model," *J. Comput. Phys.* **426**, 109955 (2021).
- <sup>30</sup>Q. Zhang and X. P. Wang, "Phase field modeling and simulation of three-phase flow on solid surfaces," *J. Comput. Phys.* **319**, 79–107 (2016).
- <sup>31</sup>S. Cui and J. Zhu, "A new finite volume multi-resolution central WENO scheme for Navier-Stokes equations on staggered meshes," *Comput. Methods Appl. Mech. Eng.* **393**, 114822 (2022).
- <sup>32</sup>T. K. Sengupta, G. Ganerwal, and A. Dipankar, "High accuracy compact schemes and Gibbs' phenomenon," *J. Sci. Comput.* **21**, 253–268 (2004).
- <sup>33</sup>P. E. Vincent, P. Castonguay, and A. Jameson, "A new class of high-order energy stable flux reconstruction schemes," *J. Sci. Comput.* **47**, 50–72 (2011).
- <sup>34</sup>W. H. Zurek, U. Dorner, and P. Zoller, "Dynamics of a quantum phase transition," *Phys. Rev. Lett.* **95**, 105701 (2005).
- <sup>35</sup>Y. Li, K. Wang, Q. Yu, Q. Xia, and J. Kim, "Unconditionally energy stable schemes for fluid-based topology optimization," *Commun. Nonlinear Sci.* **111**, 106433 (2022).
- <sup>36</sup>Q. Xia, G. Sun, Q. Yu, J. Kim, and Y. Li, "Thermal-fluid topology optimization with unconditional energy stability and second-order accuracy via phase-field model," *Commun. Nonlinear Sci.* **116**, 106782 (2023).
- <sup>37</sup>Q. Yu, Q. Xia, and Y. Li, "A phase field-based systematic multiscale topology optimization method for porous structures design," *J. Comput. Phys.* **466**, 111383 (2022).
- <sup>38</sup>Y. Li, Q. Xia, C. Lee, S. Kim, and J. Kim, "A robust and efficient fingerprint image restoration method based on a phase-field model," *Pattern Recognit.* **123**, 108405 (2022).
- <sup>39</sup>J. Wang, Q. Xia, and B. Xia, "Fast image restoration method based on the  $L_0$ ,  $L_1$ , and  $L_2$  gradient minimization," *Mathematics* **10**, 3107 (2022).
- <sup>40</sup>K. Deckelnick, G. Dziuk, and C. M. Elliott, "Computation of geometric partial differential equations and mean curvature flow," *Acta Numer.* **14**, 139–232 (2005).
- <sup>41</sup>X. Tong, C. Beckermann, A. Karma, and Q. Li, "Phase-field simulations of dendritic crystal growth in a forced flow," *Phys. Rev. E* **63**, 061601 (2001).
- <sup>42</sup>Y. Li, K. Qin, Q. Xia, and J. Kim, "A second-order unconditionally stable method for the anisotropic dendritic crystal growth model with an orientation-field," *Appl. Numer. Math.* **184**, 512–526 (2023).
- <sup>43</sup>P. T. Yue, C. Zhou, and J. Feng, "Spontaneous shrinkage of drops and mass conservation in phase-field simulations," *J. Comput. Phys.* **223**, 1–9 (2007).
- <sup>44</sup>Z. Guo, P. Lin, and J. S. Lowengrub, "A numerical method for the quasi-incompressible Cahn-Hilliard-Navier-Stokes equations for variable density flows with a discrete energy law," *J. Comput. Phys.* **276**, 486–507 (2014).
- <sup>45</sup>Y. Li, J. I. Choi, and J. Kim, "A phase-field fluid modeling and computation with interfacial profile correction term," *Commun. Nonlinear Sci.* **30**, 84–100 (2016).
- <sup>46</sup>V. Joshi and R. K. Jaiman, "An adaptive variational procedure for the conservative and positivity preserving Allen-Cahn phase-field model," *J. Comput. Phys.* **366**, 478–504 (2018).
- <sup>47</sup>L. Zheng, S. Zheng, and Q. Zhai, "Multiphase flows of N immiscible incompressible fluids: Conservative Allen-Cahn equation and lattice Boltzmann equation method," *Phys. Rev. E* **101**, 013305 (2020).
- <sup>48</sup>J. Kim, S. Lee, and Y. Choi, "A conservative Allen-Cahn equation with a space-time dependent Lagrange multiplier," *Int. J. Eng. Sci.* **84**, 11–17 (2014).
- <sup>49</sup>D. Lee and J. Kim, "Comparison study of the conservative Allen-Cahn and the Cahn-Hilliard equations," *Math. Comput. Simul.* **119**, 35–56 (2016).
- <sup>50</sup>J. Rubinstein and P. Sternberg, "Nonlocal reaction-diffusion equations and nucleation," *IMA J. Appl. Math.* **48**, 249–264 (1992).
- <sup>51</sup>M. Brassel and E. Bretin, "A modified phase field approximation for mean curvature flow with conservation of the volume," *Math. Methods Appl. Sci.* **34**, 1157–1180 (2011).
- <sup>52</sup>Y. Yu, D. Liang, and H. Liu, "Lattice Boltzmann simulation of immiscible three-phase flows with contact-line dynamics," *Phys. Rev. E* **99**, 013308 (2019).

- <sup>53</sup>E. Washburn, “The dynamics of capillary flow,” *Phys. Rev.* **17**, 273 (1921).
- <sup>54</sup>P. H. Chiu and Y. T. Lin, “A conservative phase field method for solving incompressible two-phase flows,” *J. Comput. Phys.* **230**, 185–204 (2011).
- <sup>55</sup>F. D. Vuyst, C. Fochesato, V. Mahy, R. Motte, and M. Peybernes, “A geometrically accurate low-diffusive conservative interface capturing method suitable for multimaterial flows,” *Comput. Fluids* **227**, 104897 (2021).
- <sup>56</sup>E. Olsson, G. Kreiss, and S. Zahedi, “A conservative level set method for two phase flow II,” *J. Comput. Phys.* **225**, 785–807 (2007).
- <sup>57</sup>P. H. Chiu, “A coupled phase field framework for solving incompressible two-phase flows,” *J. Comput. Phys.* **392**, 115–140 (2019).
- <sup>58</sup>Z. Huang, G. Lin, and A. M. Ardekani, “A consistent and conservative volume distribution algorithm and its applications to multiphase flows using Phase-Field models,” *Int. J. Multiphase Flow* **142**, 103727 (2021).
- <sup>59</sup>J. Qiu and C. W. Shu, “On the construction, comparison, and local characteristic decomposition for high-order central WENO schemes,” *J. Comput. Phys.* **183**, 187–209 (2002).
- <sup>60</sup>Z. Huang, G. Lin, and A. M. Ardekani, “A mixed upwind/central WENO scheme for incompressible two-phase flows,” *J. Comput. Phys.* **387**, 455–480 (2019).
- <sup>61</sup>J. B. Bell, P. Colella, and H. M. Glaz, “A second-order projection method for the incompressible Navier-Stokes equations,” *J. Comput. Phys.* **85**, 257–283 (1989).
- <sup>62</sup>W. J. Rider and D. B. Kothe, “Reconstructing volume tracking,” *J. Comput. Phys.* **141**, 112–152 (1998).
- <sup>63</sup>Q. Xia, J. Kim, and Y. Li, “Modeling and simulation of multi-component immiscible flows based on a modified Cahn-Hilliard equation,” *Eur. J. Mech. B. Fluids* **95**, 194–204 (2022).
- <sup>64</sup>X. Yuan, B. Shi, C. Zhan, and Z. Chai, “A phase-field-based lattice Boltzmann model for multiphase flows involving N immiscible incompressible fluids,” *Phys. Fluids* **34**, 023311 (2022).